

**STUDY OF MASS TRANSPORT IN ELECTRO FLUID DYNAMIC DEVICES**

by

Su Wang

B.Eng., Beijing Institute of Technology, 2013

LL.B., Beijing Institute of Technology, 2013

M.Sc., University of Saskatchewan, 2016

A THESIS SUBMITTED IN PARTIAL FULFILLMENT OF

THE REQUIREMENTS FOR THE DEGREE OF

MASTER OF APPLIED SCIENCE

in

THE FACULTY OF GRADUATE AND POSTDOCTORAL STUDIES

(Electrical and Computer Engineering)

THE UNIVERSITY OF BRITISH COLUMBIA

(Vancouver)

September 2019

© Su Wang, 2019

The following individuals certify that they have read, and recommend to the Faculty of Graduate and Postdoctoral Studies for acceptance, a thesis entitled:

Study of mass transport in electro fluid dynamic devices

---

submitted by SU WANG in partial fulfillment of the requirements for

the degree of MASTER OF APPLIED SCIENCE

in ELECTRICAL AND COMPUTER ENGINEERING

**Examining Committee:**

ROBIN F.B. TURNER, ELECTRICAL AND COMPUTER ENGINEERING

Supervisor

DAVID D.Y. CHEN, CHEMISTRY

Supervisory Committee Member

KAREN CHEUNG, ELECTRICAL AND COMPUTER ENGINEERING

Supervisory Committee Member

**Additional Supervisory Committee Members:**

MU CHIAO, MECHANICAL ENGINEERING

Supervisory Committee Member

NICOLAS JAEGER, ELECTRICAL AND COMPUTER ENGINEERING

Supervisory Committee Member

## Abstract

Mass transport in one dimensional (1D) and two-dimensional (2D) electro-fluid dynamic devices for chemical separation is systematically studied. For 1D EFD devices, like capillary electrophoresis (CE), adding external pressure during the process usually results in unwanted band broadening. However, frontal analysis (FA) can potentially benefit from the external pressure by significantly reducing the amount of time needed for analysis. Therefore, the possible impact of the pressure-assisted capillary electrophoresis frontal analysis (PACE-FA) is studied. With a typical CE-FA set-up and a typically used length and internal diameter of the capillary used, it was found that the detected concentrations of analyte will not be significantly affected by an external pressure less than 5 psi in the simulation model. In addition, the measured ligand concentration in PACE-FA was also not affected by common variables such as molecular diffusion coefficient and capillary length within the tested range. By using PACE-FA to study the binding interactions between hydroxypropyl  $\beta$ -cyclodextrin (HP- $\beta$ -CD) and small ligand molecules, the binding constants determined by CE-FA ( $18.3 \pm 0.8 \text{ M}^{-1}$ ) and PACE-FA ( $16.5 \pm 0.5 \text{ M}^{-1}$ ) are found to be similar. Based on the experimental results, it is concluded that PACE-FA can reduce the time of binding analysis while maintaining the accuracy of the measurements. For 2D-EFD device, an EFD desalination chip was designed; the desalting process was then modeled (both in single-element and multiple-element geometric design) and was simulated. The simulation results showed that the ionic components were separated and outflowed to specific channels as designed which suggests a potential alternative way for microscale-desalination. The result of this study also showed that the performance of the device relied on the geometry of the device relatively heavily and can be improved by applying a stronger electric field at the electrodes.

## **Lay Summary**

This work presents two studies on mass transport in Electro-Fluidic-Dynamic (EFD) devices. A pressure-assisted capillary electrophoresis frontal analysis (PACE-FA) system is studied both theoretically and experimentally and was found that it can reduce the time of the binding analysis while maintaining the accuracy of the measurements. This approach could potentially become a more common tool for the analysis of bio-molecular interactions in the future. In the second project, a micro-fluidic chip-based device was designed and studied for desalination applications, which can be of significance utility for desalting not only for the seawater reuse but also for the biological sample pre-treatment for mass spectrometry applications.

## **Preface**

The thesis presents the research performed by the author, under the supervision of Prof. David Da Yong Chen and Prof. Robin Turner. The author conducted all the computational modeling of COMSOL Multiphysics in the thesis and a published journal paper is an original intellectual produce of the author and the other co-first author Cheng Qian, with the guidance and supervision of Prof. David Da Yong Chen.

The contribution from other researchers and collaborators are detailed below.

### **Contribution from other researchers:**

#### Chapter 2:

The CE-FA experiment was performed with Cheng Qian, Hengqing Fu, on which Cheng Qian and the author contributed equally to the work including drafting, editing and revision. The work was done under supervision and guidance of Prof. David Da Yong Chen, Prof. Huihui Li and Prof. Robin Turner. A version of this chapter has been published as:

\*Qian, C., \*Wang, S., Fu, H., Turner, R. F., Li, H. and Chen, D. D. (2018), Pressure-assisted capillary electrophoresis frontal analysis for faster binding constant determination. *ELECTROPHORESIS*, 39: 1786-1793.

The published journal paper was written mainly by the Cheng Qian and the author, with feedback and suggestions by Prof. David Da Yong Chen.

#### Chapter 3:

The work is done by the author, with the supervision of Prof. David Da Yong Chen as well as the guidance of Prof. Robin Turner.

## Table of Contents

<b>Abstract.....</b>	<b>iii</b>
<b>Lay Summary .....</b>	<b>iv</b>
<b>Preface.....</b>	<b>v</b>
<b>Table of Contents .....</b>	<b>vi</b>
<b>List of Tables .....</b>	<b>ix</b>
<b>List of Figures.....</b>	<b>x</b>
<b>List of Abbreviations .....</b>	<b>xiv</b>
<b>List of Symbols .....</b>	<b>xv</b>
<b>Acknowledgements .....</b>	<b>xvi</b>
<b>Dedication .....</b>	<b>xviii</b>
Chapter 1: Introduction and Overview.....	1
1.1        Separative transport and mass transfer equation .....	1
1.2        Desalination and microfluidic desalination techniques.....	3
1.2.1    Macro-scale desalination techniques.....	3
1.2.2    Microfluidic desalination techniques .....	5
1.3        Electro fluid dynamic devices and working principle.....	11
1.4        Research objective .....	13
Chapter 2: Simulation for Pressure-Assisted Capillary Electrophoresis Frontal Analysis (1D EFD Device).....	14
2.1        Introduction .....	14
2.2        Theory .....	15
2.2.1    Applying external pressure to CE-FA.....	15

2.2.2	Limits of applied pressure and the injected sample plug length .....	18
2.3	Materials and methods .....	22
2.3.1	Chemicals and sample preparation.....	22
2.3.2	Instrumentation.....	22
2.3.3	Simulation .....	23
2.4	Results and discussion.....	23
2.4.1	COMSOL Multiphysics® simulation .....	23
2.4.2	Using PACE-FA to achieve faster and equally accurate analysis.....	26
2.4.3	Using PACE-FA to analyze the interaction between molecular species with opposite charges in a neutral-coated capillary .....	30
2.5	Conclusion.....	31
Chapter 3: 2D-EFD Design and Simulation Result .....		32
3.1	EFD desalination design .....	32
3.1.1	2D-EFD working principle and workflow of the simulation .....	33
3.1.2	Geometry, design, numerical solutions and simulation .....	36
3.1.3	Results and discussion.....	39
3.2	EFD desalination design vs electric potential .....	47
3.2.1	Geometry, design, numerical solutions and simulation .....	47
3.2.2	Results and discussion.....	48
3.3	Multi-element EFD in parallel vs electric potential .....	51
3.3.1	Introduction .....	51
3.3.2	Results and discussion.....	53

3.4	Multi-element EFD in parallel with a longer injection channel length vs electric potential.....	57
	3.4.1 Introduction.....	57
	3.4.2 Results and discussion.....	58
3.5	Multi-element EFD in parallel with injection channel width changed vs electric potential.....	61
	3.5.1 Introduction.....	61
	3.5.2 Results and discussion.....	62
Chapter 4: Conclusions and Suggestions for Future Work.....		65
4.1	Conclusions.....	65
4.2	Future work.....	66
<b>Bibliography.....</b>		<b>69</b>

## List of Tables

Table 2.1 The comparison of binding constants determined from CE-FA/PACE-FA .....	30
Table 3.1 Dimensions and parameter settings for EFD desalination model.....	38
Table 3.2 Dimensions and parameter settings for EFD desalination model. The changes compared to Table 3.1 are highlighted in green. ....	47
Table 3.3 Dimensions and parameter settings for the model of three EFD devices in parallel....	52
Table 3.4 Dimensions and parameter settings used to define the model of the three EFD devices in parallel with a longer injection length. The changes are highlighted in green. ....	57
Table 3.5 Dimensions and parameter settings for the model of three EFD devices in parallel with injection width changed. The changes are highlighted in green. ....	61

## List of Figures

Figure 1.1 Schematic of the principles of the desalination techniques. (a) Multi-stage flash distillation (MSF) and multi-effect distillation (MED); (b) electro dialysis (ED); (c) reverse osmosis (RO). Redrawn based on the [8] [11] [12] [13].	4
Figure 1.2 Schematic of the principles of the microfluidic desalination techniques. (a) Dialysis; (b) Capacitive deionization (CDI); (c) Ion concentration polarization (ICP); (d) Electrochemical desalination (ECD). Redrawn based on the [18] [28] [31] [33].	6
Figure 1.3 The schematic of the CDI process. Redrawn based on the fundamentals of the CDI process. (a) Electrostatic adsorption; (b) Regeneration. A CDI unit consists of two pairs of oppositely charged porous electrodes that could be further assembled into CDI stacks with multiple electrodes.	9
Figure 1.4 Schematics of the setup. Reprinted from the paper [1]: (a) channel geometry of the microfluidic EFD device and (b) a schematic of the device made from a 2.54 cm × 7.62 cm PDMS chip.	12
Figure 2.1 Numerical results of the solute concentration distribution in the channel with different external pressures applied at the inlet.	24
Figure 2.2 Numerical results of the solute concentration in the channel with (A) different solute diffusion coefficient; (B) different total channel length for particles with a diffusion coefficient of $10^{-9} \text{m}^2/\text{s}$ ; (C) different sample plug length to channel length ratio with particles used in (B). All simulations were performed under 1 psi per 50 cm capillary length, the same as what was used in the real experiment.	25
Figure 2.3 CE-FA electropherogram of HP- $\beta$ -CD and benzoate interaction. (A) Analyzed under 15 kV; (B) Analyzed under 15 kV with 1psi pressure applied on the inlet side.	27

Figure 2.4 The standard calibration curves of benzoate obtained under 0 psi+15 kV, 1 psi+15 kV and 2 psi+15 kV.....	28
Figure 2.5 Comparison of binding isotherms determined with CE-FA and PACE-FA. (A) HP- $\beta$ -CD with benzoate; (B) HP- $\beta$ -CD with para-nitrophenol.....	29
Figure 3.1 Schematic drawing of the geometry of the EFD desalination design (on the x-y plane). The electrodes are placed at A1B1, B1C1, D1E1, A2B2, B2C2 and D2E2 respectively. ....	32
Figure 3.2 Different geometry of the EFD desalination design: Type 1 (on the left) vs Type 2 (on the right).....	33
Figure 3.3 Workflow of the simulation.....	36
Figure 3.4 EFD device schematic model in COMSOL. The samples flow into the surface defined by zw and xw and outflow through the three channel arms at the opposite end of the device.....	37
Figure 3.5 EFD electric potential distribution for the Type 2 geometry. ....	40
Figure 3.6 Velocity distribution inside the EFD device (front view). ....	40
Figure 3.7 Concentration distribution of the sodium ions inside the EFD device at different times (front view). a) time=0sec; b) time=60 sec; c) time=120 sec; d) time=180 sec; e) time=240 sec; f) time=360 sec; g) time =600 sec; h) time=1200 sec; i) time=3600 sec. The electrode voltages were $V = \pm 20V$ . ....	42
Figure 3.8 Concentration distribution of the chloride ions inside the EFD device at the different times (front view). a) time=0sec; b) time=60 sec; c) time=120 sec; d) time=180 sec; e) time=240 sec; f) time=360 sec; g) time =600 sec; h) time=1200 sec; i) time=3600 sec. The electrode voltages were $V = \pm 20V$ . ....	43
Figure 3.9 Concentration distribution of the neutral component inside the EFD device at different times (front view). a) time=0sec; b) time=60 sec; c) time=120 sec; d) time=180 sec; e) time=240	

sec; f) time=360 sec; g) time =600 sec; h) time=1200 sec; i) time=3600 sec. The electrode voltages were  $V = \pm 20V$  ..... 44

Figure 3.10 Average surface concentration at the very end of the EFD device side exit channels (cross-sectional). a) left-side exit channel (channel 1); b) right-side exit channel (channel 3). The electrode voltages were  $V = \pm 20V$  ..... 45

Figure 3.11 Average surface concentration at the very end of the EFD device main exit channel (cross-sectional). The electrode voltages were  $V = \pm 20V$  ..... 46

Figure 3.12 Average concentrations at the very end of the side exit channel 1 (cross-sectional) based on different electric potentials applied to the electrodes. The electrode voltages were  $V = \pm 10V, \pm 15V, \pm 20V, \pm 25V$  and  $\pm 30V$  ..... 48

Figure 3.13 Average concentrations at the very end of the side exit channel 3 (cross-sectional) based on different electric potentials applied to the electrodes. The electrode voltages were from  $V = \pm 10V, \pm 15V, \pm 20V, \pm 25V$  and  $\pm 30V$  ..... 50

Figure 3.14 Average concentrations at the very end of the main exit channel 2 (cross-sectional) based on different electric potentials applied to the electrodes. The electrode voltages were  $V = \pm 10V, \pm 15V, \pm 20V, \pm 25V$  and  $\pm 30V$  ..... 51

Figure 3.15 Schematic model of three EFD elements connected in parallel as defined for simulation in COMSOL. The samples inflow at the bottom surface ( $y = 0$ ) and outflow through the three channels as for the single device considered above. .... 52

Figure 3.16 Average concentrations at the very end of the side exit channel 1 (cross-sectional) based on different electric potentials applied to the electrodes. The electrode voltages were  $V = \pm 10V, \pm 15V$  and  $\pm 20V$  ..... 53

Figure 3.17 Average concentrations at the very end of the side exit channel 3 (cross-sectional) based on different electric potential applied to the electrodes. The electrode voltages were  $V = \pm 10V, \pm 15V$  and  $\pm 20V$ ..... 55

Figure 3.18 Average concentrations at the very end of the main exit channel 2 (cross-sectional) based on different electric potential applied to the electrodes. The electrode voltages were  $V = \pm 10V, \pm 15V$  and  $\pm 20V$ ..... 56

Figure 3.19 Average concentrations at the very end of the side exit channel 1 based on different electric potentials applied to the electrodes for the case of a longer injection channel length. The electrode voltages were  $V = \pm 10V, \pm 15V$  and  $\pm 20V$ ..... 58

Figure 3.20 Average concentration at the very end of the side exit channel 3 based on different electric potentials applied to the electrodes for the case of a longer injection channel length). The electrode voltages were  $V = \pm 10V, \pm 15V$  and  $\pm 20V$ ..... 59

Figure 3.21 Average concentration at the very end of the main exit channel 2 based on different electric potentials applied to the electrodes for the case of a longer injection channel length. The electrode voltages were  $V = \pm 10V, \pm 15V$  and  $\pm 20V$ ..... 60

Figure 3.22 Average concentrations at the very end of the side exit channel 1 based on different electric potentials applied to the electrodes for the case where the injection channel width is larger. The electrode voltages are  $V = \pm 10V, \pm 15V$  and  $\pm 20V$ ..... 62

Figure 3.23 Average concentrations at the very end of the main exit channel 2 based on different electric potentials applied to the electrodes for the case where the injection channel width is larger. The electrode voltages were  $V = \pm 10V, \pm 15V$  and  $\pm 20V$ ..... 63

## List of Abbreviations

CDI	capacitive deionization
CE	capillary electrophoresis
ED	electrodialysis
EFD	electro-fluid-dynamic
EOF	electroosmotic flow
ECD	electrochemical desalination
FCCE	flow counterbalanced capillary electrophoresis
FA	frontal analysis
HP- $\beta$ -CD	hydroxypropyl beta cyclodextrin
ICP	ion concentration polarization
MS	mass spectrometry
MED	multi-effect distillation
MSF	multi-stage flash distillation
PDMS	polydimethylsiloxane
PACE	pressure assisted capillary electrophoresis
RO	reverse osmosis
Re	Reynold number
UV	ultraviolet

## List of Symbols

$\bar{E}$	applied electrical field
$\mu_i$	apparent mobility of the ion $i$
$c$	concentration
$c_{z,t,i}$	concentration of the ion $i$ at the position $z$ and time $t$
$D$	diffusion coefficient
$W$	direct displacement velocities
$r$	distance to the center line for any given point
$\eta$	dynamic viscosity of the solution
$v_{eo}$	electroosmotic velocity
$J$	flux density
$a$	inner radius of the capillary
$U$	impelling solute velocity driven by the chemical potential gradients
$v_0$	maximum axial velocity of analyte
$v_f$	net fluid velocity
$\Delta P$	pressure difference between ends of the capillary
$v_p$	pressure-induced velocity
$L_t$	total length of the capillary
$Z$	total length of the sample plug
$v$	velocity
$Q$	volumetric flow rate

## Acknowledgements

There are quite a few individuals who support and encourage me during this graduate program, which help me make this work possible.

First and foremost, I wish to thank Prof. Robin Turner and Prof. David (Dayong) Chen for their roles as my supervisors. I am grateful for the limited time and efforts they devoted in my research and program. Without their guidance, this dissertation would not have been possible.

I could not express enough thanks to my advisory committees, Prof. Mu Chiao from mechanical engineering, Prof. Nicolas Jaeger from electrical and computer engineering and Prof. Karen Cheung from biomedical engineering.

I am grateful to all the professors who I have taken courses from, Prof. Edmond Cretus, Prof. Michael Blades and Prof. James Feng; moreover, I will not forget the experience being Teaching Assistant with all the course instructors who I worked for, including Prof. Siamak Najarian, Prof. Anthony Chan, Prof. Guillaume Bussiere, Prof. Carol Jaeger and Prof. Philip Loewen.

In addition, my sincere thanks go to all my classmates, lab mates and colleagues in the Michael Smith Building (MSL), Department of Electrical & Computer Engineering (EECE) and Department of Chemistry (CHEM), who makes my life at UBC joyful, including but not limited to: Chang Liu, Akram Khodabandehloo, Jessica (Risley) McGregor, Cheng Qian, Matthew MacLennan, Kevin Kovalchik, Caitlyn Grypma, Lingyu Wang, Jianhui Cheng, Zi-Ao Huang, Wenqiang Jing, Yuri Chenyakin,, Julie Mcnutt, Adam Kowalczyk, Xianzhe (Xander) Yin, Tingting Zhao from David's lab; Tony (Chengwei) Yang, Stanislav(Stas) Konorov, Chad Atkins, George Schulze and Martha Vardaki from Robin's lab; Shreyas Rangan, Niki Sabour, Katrin

Braasch, Cagri Kocyigit, Alina Kunitskaya, Rene Pedroza Lozano, Chris Sherwood from James Piret's lab; Hao Ding, Fennie Easton van der Graaf, Nicholas McGregor, Stephen MacDonald, Vince Tingey, Guillaume Déjean, Gregory Arnal, Sean McDonald, Roderick Xia from MSL; Chang Ge, Qi Zeng, Manyou Ma, Melika Shahriari, Minglei Ma, Yi Luo, Enxiao Luan, Zhonghua (Sebastian) Zhou, Mengye Cai from EECE; Anthony Chan, Manish Vashishta, Arshdeep Gill, Matei Vacariu, Jiayu (Jeff) Li, Youping Li, Tianyu Duan from CHEM; Nodir Kodirov, Bill Cheng, Guangyi Cao, Zhiqiang Wu, Zhiguo Zhang, Zicong Hu, Shan Jiang, Qi (Patrick) Pan, Kui Pan, Zhiming Wu, Zhongshou Wu, Xiaoyu (Grace) Zhou.

Thanks to all the other friends and great people who I met in Metro Vancouver.

Thanks to my family for their endless love and support throughout my life. Their unwavering support is what allowed me to achieve my goals.

## Dedication

- Just wait and see.
- Maybe this is the end of my journey in school but won't be the end of my learning.
- Dedicated to my beloved.

## **Chapter 1: Introduction and Overview**

Purification of biological materials such as lipids, DNA, proteins, and metabolites under physiological conditions is important in many areas of biomedical research. Current technologies used to purify the materials mentioned (e.g. liquid chromatography, two-dimensional gel electrophoresis) often require denaturation of biomolecules and usually are incapable of processing large amounts of material. Capillary electrophoresis, whose working principle is based on the differential mobility of charged species in an applied electric field, can be used to separate species which are not easily resolved by other methods. However, limited by the physical dimensions of the capillary columns, fraction collection of CE generally produces only small amounts of purified sample components. More recently, two-dimensional electro-fluid dynamic (2-D EFD) devices have utilized hydrodynamic pressure, as well as an electric field, to drive analyte and fluid migration through the two-dimensional channel networks (as opposed to the one-dimensional columns of CE). The 2-D EFD devices have shown the potential to continuously purify multiple components from complex samples into different channels, each containing a substantially pure compound, as described in several publications [1]–[4]. The main purpose of this project is to study the mass transport behavior in EFD devices for applications involving desalination of the sample or purification of biomolecules.

### **1.1 Separative transport and mass transfer equation**

The development of separation science has been one of the most important contributing factors in modern analytical chemistry, particularly for the life sciences. Without effective separation techniques, enzyme purification, DNA and protein sequencing [5], [6], efficacy or metabolite studies in the pharmaceutical industry, and insights into many chemical and

biological reactions would have not advanced to what they are nowadays. The ultimate goal of many separation studies is to obtain a description of how component concentrate pulses move in relationship to one another. In one dimension, these movements are governed by the equation shown below which is the basic expression for molar flux density:

$$J = Wc - D \frac{dc}{dz} \quad (\text{Equation 1.1})$$

where  $J$  denotes the flux density [mol/(m<sup>2</sup>\*s)];  $c$  denotes the concentration [mol/m<sup>3</sup>];  $D$  is the diffusion coefficient [m<sup>2</sup>/s]. The quantity  $W$  herein represents the sum of all the direct displacement velocities [m/s], those caused by bulk displacement at velocity  $v$  [m/s] plus those caused by chemical potential gradients which impel solute at velocity  $U$  [m/s]. Thus  $W$  is given by

$$W = U + v \quad (\text{Equation 1.2})$$

The basic equation for concentration changes are described by the so-called the general form of the mass transfer equation as shown below.

$$\frac{\partial c}{\partial t} = -(U + v) \frac{\partial c}{\partial z} + D \frac{\partial^2 c}{\partial z^2} = -W \frac{\partial c}{\partial z} + D \frac{\partial^2 c}{\partial z^2} \quad (\text{Equation 1.3})$$

where  $W$  symbolizes the total of all non-diffusional displacement velocities as described above.

For capillary electrophoresis (CE), the mass transport process can be described by the partial differential equation shown below.

$$\frac{\partial c_{z,t,i}}{\partial t} = -\mu_i E_z \frac{\partial c_{z,t,i}}{\partial z} + D_i \frac{\partial^2 c_{z,t,i}}{\partial z^2} \quad (\text{Equation 1.4})$$

where  $c_{z,t,i}$  is the concentration of the ion  $i$  at the position  $z$  [m] and time  $t$  [s];  $E_z$  is the total local electric field strength [V/m];  $\mu_i$  is the apparent mobility [ $\text{m}^2/(\text{s}*\text{V})$ ] of the ion  $i$ ;  $D_i$  is the diffusion coefficient [ $\text{m}^2/\text{s}$ ] of the ion  $i$ .

It is worthy to note that the  $-\mu_i E_z \frac{\partial C_{z,t,i}}{\partial z}$  part is due to electrophoretic migration while the  $D_i \frac{\partial^2 C_{z,t,i}}{\partial z^2}$  part is due to the molecular diffusion.

## 1.2 Desalination and microfluidic desalination techniques

### 1.2.1 Macro-scale desalination techniques

Conventionally, desalination is a process that has been proposed as a solution for reducing the world-wide drinking water shortage [7], [8], which includes a series of established methods for drinking water production from salt water. Typically, it is applied on the macro-scale for drinking water production from seawater or brackish water. Generally, the average salinity of seawater is  $35 \text{ g/L}$ , which means that for every 1 litre of seawater there are 35 grams of salts (mostly, but not entirely, sodium chloride) dissolved in it [9], while the salinity of brackish water is around 1 to  $10 \text{ g/L}$  [10]. As regards to drinking water (known as potable water), the salinity should be less than  $1 \text{ g/L}$  [10]. Water recovery rate is one of the most frequently mentioned performance indicators for desalination, which is defined as the ratio of the flow-rate of fresh water produced to the flow-rate of the influent stream.

To date, the most commonly implemented desalination techniques include multi-stage flash distillation (MSF) and multi-effect distillation (MED) [11], electrodialysis (ED) and reverse

osmosis (RO) [8], [12]. The working principles for each technique are depicted in Figure 1.1 below.

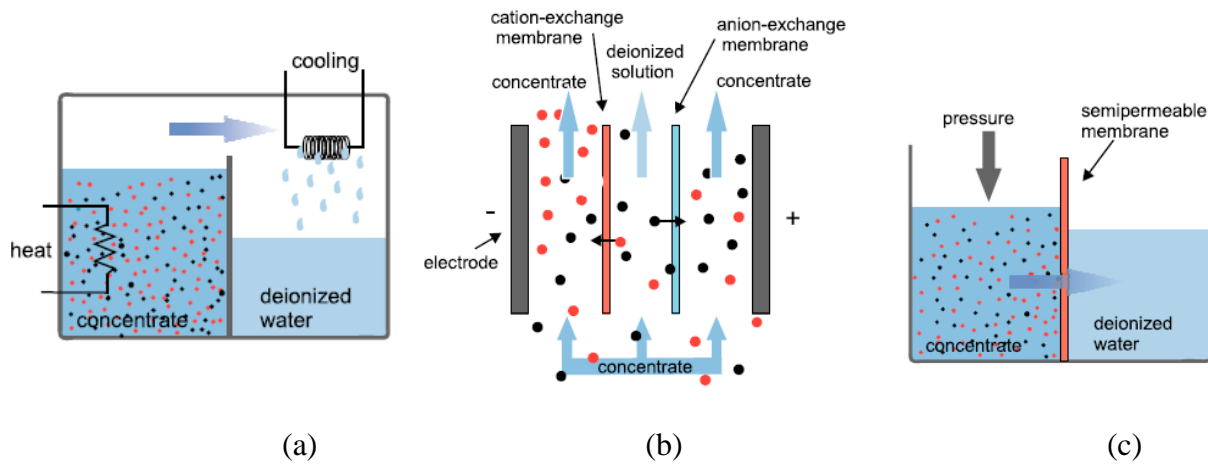


**Figure 1.1 Schematic of the principles of the desalination techniques. (a) Multi-stage flash distillation (MSF) and multi-effect distillation (MED); (b) electrodialysis (ED); (c) reverse osmosis (RO). Redrawn based on the [8] [11] [12] [13].**

MSF and MED are based on thermal desalination, where water is evaporated through the input of heat and condenses in a fresh water reservoir [11]. The basic principle of electrodialysis [13] is to place two electrodes in parallel with alternating cation and anion exchange membranes. The elements are separated through spacers, where the potential is applied across the stack. The ions in the electrolyte enter and transport through the membranes until they are blocked. Cations can only pass through the cation selective membranes, while anions can only pass through anion selective membranes. As a result, concentrated streams can be obtained [7]. RO is based on an over-pressure on the concentration side of a semipermeable membrane [14]. The typical recovery rate of RO is from 35% to 85%, which depends on the composition and concentration of the feed solution [13].

Among these three existing techniques, RO is the most favored method for desalination facilities built within the last two decades [14] because of its energy efficiency for desalination of seawater. But, admittedly, thermal methods and RO are energy intensive processes, due to either high temperatures (MSF and MED) or high pressures (RO). Electrodialysis can reach a recovery percentage of 94% and the energy consumption of electrodialysis is  $0.4\sim 8.7 \text{ kWh} * \text{m}^{-3}$  [15]. According to Ghaffour et al. [16], the typical energy consumption of RO desalination plant for seawater and brackish water is  $3\sim 4$  and  $0.5\sim 2.5 \text{ kWh} * \text{m}^{-3}$ , respectively. Therefore, it can be concluded that electrodialysis is competitive in terms of energy efficiency for desalination of brackish water [17].

### **1.2.2 Microfluidic desalination techniques**

Electrodialysis systems can easily be implemented on a large enough scale for drinking water applications. In contrast, microfluidic desalination (with two dimensions in the sub-millimeter scale and flow rates in the order of Nano-liter to micro-liter per minute) serves as an alternative technology for small scale applications and offers new opportunities for lab-on-chip devices (for example, as a tool for sample preparation for mass spectrometry). The down-scaling analysis with microfluidic desalination has several advantages including operation speed, reduction of sample losses, lower potential for contamination and high reproducibility. Moreover, studies of desalination-on-chip systems may help to better understand ion transport in existing (larger scale) desalination devices (like desalination recovery and speed).

Currently, common microfluidic desalination techniques include dialysis [18]–[21], electrodialysis (ED) [21], capacitive deionization (CDI) [22], [23], ion concentration polarization

(ICP) [24], [25] and electrochemical desalination (ECD). The operation principles for each microfluidic technique are depicted in Figure 1.2 and further described below.

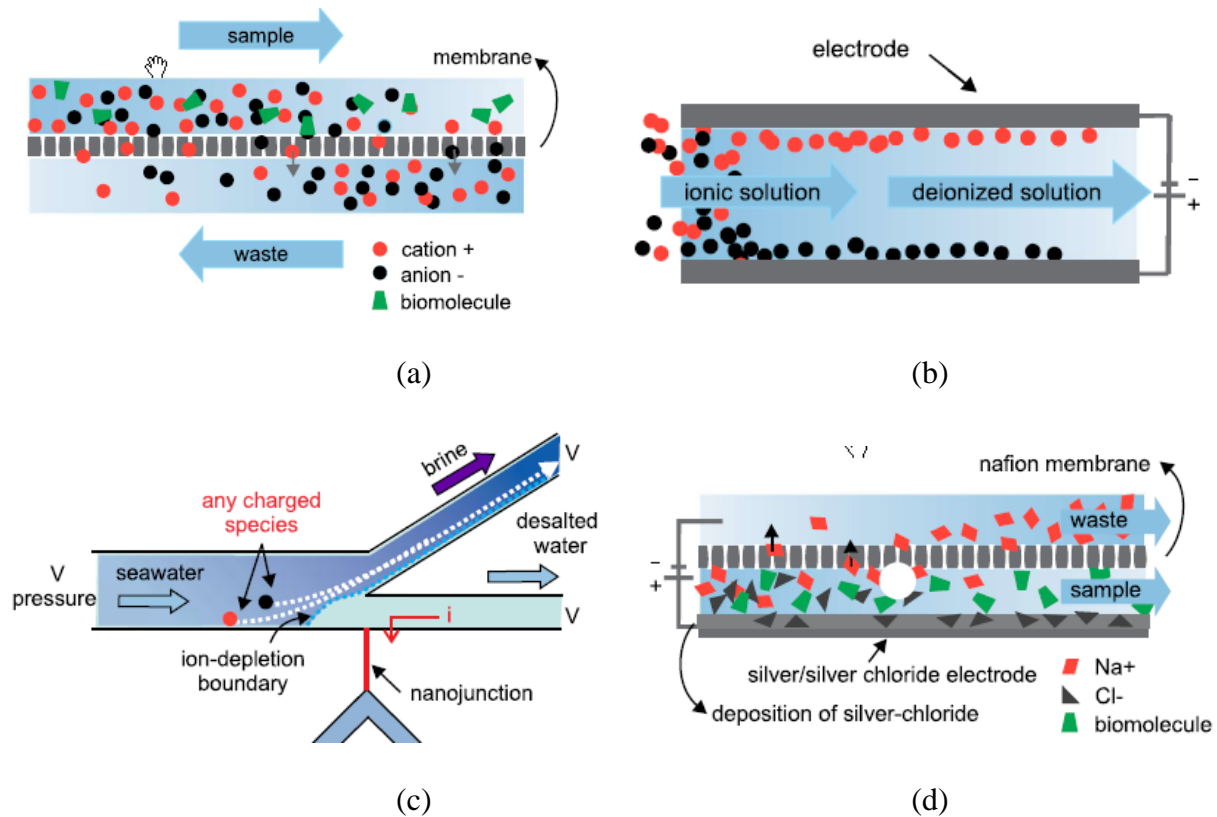


**Figure 1.2 Schematic of the principles of the microfluidic desalination techniques. (a) Dialysis; (b) Capacitive deionization (CDI); (c) Ion concentration polarization (ICP); (d) Electrochemical desalination (ECD). Redrawn based on the [18] [28] [31] [33].**

### 1.2.2.1 Dialysis

Dialysis is a separation process based on diffusion of molecules or ions through a membrane. The salt concentration of the influent stream is then diluted through the membrane into a second solvent with a low salt or zero-salt concentration. The components to be removed

diffuse across the membrane, traditionally fabricated from cellulose or poly(vinylidene fluoride) into a buffer solution [18].

The drawbacks of dialysis are that, besides the salt, also some of the compounds of interest may diffuse through the membrane into the buffer, which could result in a lower sensitivity of the analysis. The application of a membrane with a certain mechanical stability sets a limit for the pressure difference and flow-rate that can be applied. Based on the literature, micro-dialysis has been implemented on-chip and coupled to electrospray ionization mass spectrometry systems (ESI-MS) as a sample preparation method [19], [20]. However, analysis of protein or DNA-samples with a high concentration of buffers and salts can be impossible due to ion suppression (a low signal-to-noise ratio) with mass spectrometry (MS) [26], [27].

#### **1.2.2.2 Electro dialysis (ED)**

Strathmann's group reviewed electro dialysis and related processes in [17]. It can be applied for water desalination and salt preconcentration. The working principle has been described above as applied in macro-scale desalination section. Although electro dialysis may not compete with reverse osmosis (RO) in terms of energy efficiency, it can still be advantageous for applications where ion specificity or a high purity is required. The reason is the fact that the technique is scalable and does not require high pressure pumps which are required for RO. Investigation of miniaturized electro dialysis systems may contribute to optimization of the operation of large-scale ED systems (e.g. improvements of the energy efficiency) as well as to the fundamental understanding of ion transport near ion selective membranes.

Kwak et al. experimentally investigated ion transport within a polydimethylsiloxane (PDMS) ED cell [21]. NaCl solution of 10 *mM* was introduced into the system. The local salt

concentration as well as the flow profile was visualized through the addition of Rhodamine 6G which is positively charged. From their experiments, they found that the observed asymmetry in the vortices at the anion selective membrane and cation selective membrane could be explained by different Stokes radii and transport properties of the cations and anions [21].

### 1.2.2.3 Capacitive deionization (CDI)

Capacitive deionization (CDI) is an electric potential induced adsorption process on the surface of electrodes. The fundamental CDI process is based on the formation of electrical double layers (EDLs) in the proximity of electrodes as a result of applying an electric potential. The ions are electrostatically adsorbed on the EDLs and can be desorbed by removing the applied potential [28].

The CDI process has two major steps: (1) electrostatic adsorption on the EDLs, where charged ions in electrolyte solutions are forced to migrate toward opposite-charged electrodes by an imposed constant voltage or current (i.e.,  $<1$  V and  $\pm 1$  A) and (b) regeneration, where removing or reversing the applied potential (or current) results in desorption of ions and consequently regeneration of electrodes [29]. CDI can be applied either to purify water streams containing ions (e.g.,  $\text{Na}^+$ ,  $\text{Cl}^-$ ,  $\text{SO}_4^{2-}$ ,  $\text{Cu}^{2+}$  and  $\text{Ca}^{2+}$ ) for desalination and water softening applications or to remove a variety of heavy and transitional metal ions (e.g.,  $\text{Zn}^{2+}$ ,  $\text{Mn}^{2+}$ ,  $\text{Cd}^{2+}$ ,  $\text{Cd}^{3+}$ ,  $\text{Cr}^{6+}$  and  $\text{Cu}^{2+}$ ) in industrial wastewater treatment [30]. CDI has been previously employed in brackish desalination and seawater desalination, wastewater remediation, as well as water softening applications.

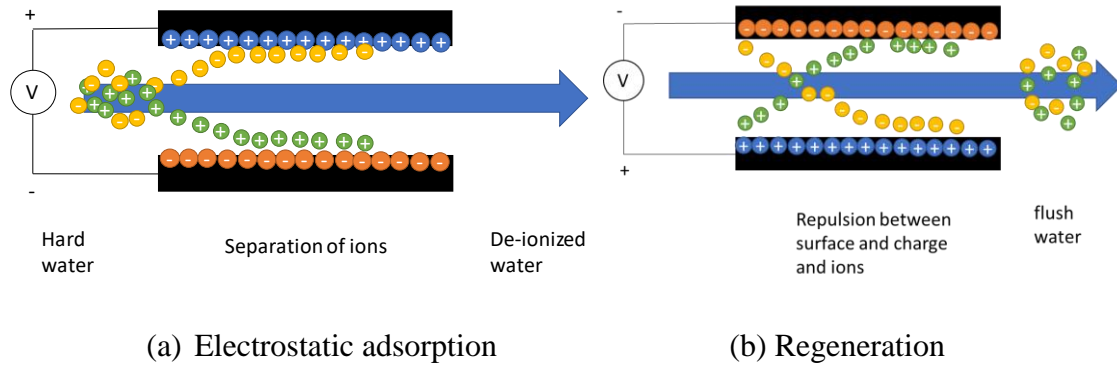


**Figure 1.3** The schematic of the CDI process. Redrawn based on the fundamentals of the CDI process. (a) Electrostatic adsorption; (b) Regeneration. A CDI unit consists of two pairs of oppositely charged porous electrodes that could be further assembled into CDI stacks with multiple electrodes.

#### 1.2.2.4 Ion concentration polarization (ICP)

Ion concentration polarization was first applied to desalinate seawater to yield fresh water by Kim's group [25]. The operational mechanism is that a current through an ion selective membrane establishes an ion depletion zone on one side of a membrane with pores of the size of approximately the Debye length. The depletion zone occurs because ions of similar charge at the walls of the nanopores present in the membrane are repelled by the membrane. The ions of opposite charge travel through the membrane pores. This results in an ion depletion zone on one side of the membrane and an ion enrichment zone on the other side of the membrane.

ICP was applied by Kim's group to desalinate water using a y-shaped microfluidic channel [31]. By passing a salt solution through the feed channel with a nanojunction located at the onset of the outlets, a desalted stream can be separated from a brine stream. The nanojunction is a nanometer sized channel or pore which connects two larger, micrometer size channels. Across the nanochannel a potential is applied and consequently, according to the above described operational mechanism, a depletion zone is established at the interface between the nanofluidic

and microfluidic channels. The result is a fresh water stream exiting at one outlet and a concentrated brine solution exiting at the second outlet. The water recovery rate observed by Kim et al. was 50% at a salt rejection rate of 99% [31].

ICP can be implemented to remove charged species from uncharged species and to separate particles and ions not on the base of their mobility. The geometry design of this method is robust. MacDonald et al. demonstrated that ICP is scalable in sample throughput. The energy consumption of the device was 4.6 and 13.8 *Wh/ L* for 20 and 200 *mM* electrolyte, respectively [24].

#### **1.2.2.5 Electrochemical desalination (ECD)**

Electrochemical desalination is based on Faradaic reactions occurring at electrodes upon a sufficiently high driving potential. By applying a potential of 3 V across a bipolar electrode, fabricated from pyrolyzed photoresist, the  $\text{Cl}^-$  present in seawater oxidizes at the anode and neutralizes. Crooks's group reported this finding in [32] by using a similar configuration that Kim's group used in ICP desalination work [24] (a nanopore for ICP to desalinate seawater). They reported that the rejection rate was  $25\pm 5\%$  of salt. While the energy consumption was 25 *mWh/ L* at a water recovery of 50%. The system is potentially energy efficient for small scale desalination facilities. Then, Grygolicz et al. implemented ECD by using a cylindrical two-electrode electrochemical desalination cell [33]. The center of the cylinder consists of a silver/silver chloride (Ag/AgCl) electrode. This is encapsulated by a Nafion membrane which is again surrounded by the solution to be desalinated. Upon the application of a positive potential, the  $\text{Cl}^-$  ions are removed from a sample solution through the oxidation of silver at the Ag/AgCl electrode which results in further silver chloride formation. The membrane is cation selective and

only passes the  $\text{Na}^+$  ions while the transport of  $\text{Cl}^-$  ions is blocked. It was demonstrated that in flow-through mode 90% of the salt is removed within 90 s with a maximum flowrate of 40  $\mu\text{L}/\text{min}$  and start concentration of 0.6 M NaCl [33].

### **1.3 Electro fluid dynamic devices and working principle**

In the 2-D EFD devices discussed in [1]–[4], analytes are driven through the fluid by non-discriminative forces (e.g., pressure or electro-osmosis) and by discriminative forces (e.g., from the applied electric field). These forces exist simultaneously and produce a net migration of analytes determined by the sum of the velocity vectors.

The basic objective of 2D-EFD devices is to separate the analytes by controlling the pressure and applied electric field when the electrophoretic mobilities of the analytes are known but not equal. For instance, in a conventional 2D-EFD devices, a positive electric potential is applied at a sample vial to drive charged analytes within the sample into and against the flow of an electrolytic fluid in a separation stream, of which the pressure-induced velocity can be precisely controlled so as to manipulate the migration of the various analytes in the same direction as, or against, the bulk flow of fluid in the separation channel due to the electrophoretic mobility of the particular analyte [1], [2].

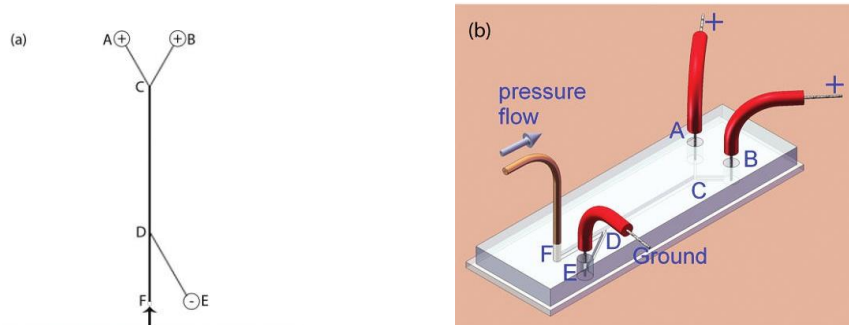


**Figure 1.4 Schematics of the setup. Reprinted from the paper [1]: (a) channel geometry of the microfluidic EFD device and (b) a schematic of the device made from a 2.54 cm × 7.62 cm PDMS chip.**

As shown in Figure 1.4 above, the EFD utilizes a fluid flow in a main separation channel into which one or more analytes can be injected utilizing an electric potential applied at a sample vial to drive charged analytes within the sample into a micro-scale channel for separation. This Y-shaped EFD shown utilizes a pressure-driven bulk fluid flow to deliver a sample fluid into the separation stream without discriminating individual analytes based on their charge status, and can provide faster sample processing, resistance to unstable electro-osmotic flow, and avoid buffer depletion that is common in 2D-EFD devices. Further, the continuous nature allows the complete processing of a mixture that is constantly introduced [34]. This device expands the geometry of separation from a one-dimensional single column to a two-dimensional complex channel networks, providing an alternative to overcome the drawback of continuous flow capillary electrophoresis.

#### **1.4 Research objective**

The main purpose of this work is to study the mass transport of ionic species in specific electro-fluidic dynamic devices (EFD devices) intended for separation applications. The specific objectives are the following:

1. Study the possible impact due to the external pressure on CE-FA by investigating the mass transfer equation along the tube. This could be helpful to better understand and model the EFD device because the analytes/ions both are transported through the fluid by pressure-driven force and electrical-field-driven force simultaneously. Moreover, this project is used to test the utility of COMSOL Multiphysics for such applications and to examine different types of flow in a simple channel.
2. Study the mass transport within a specified EFD device for desalination in a single-element design configuration and investigate the potential utility of a multi-element design configuration for improved performance and determination of suitable operating variable settings.

## Chapter 2: Simulation for Pressure-Assisted Capillary Electrophoresis

### Frontal Analysis (1D EFD Device)

#### 2.1 Introduction

Capillary electrophoresis (CE) has proven to be an analytical technique with many important applications [35]–[37]. Chiral separation [38], [39], genomics [40], metabolomics [41], [42], proteomics [43], drug discovery [44], [45] and macro molecular interaction studies are a few examples of this simple yet powerful separation technique [46], [47]. In CE, charged molecules with different electrophoretic mobility are separated under a strong electric field and in some cases all species are driven by the electroosmotic flow (EOF). Compared to the flat-shaped flow profile of the EOF-driven flow, the pressure-driven laminar flow in an open tube has a parabolic flow profile. Because this parabolic profile has a negative effect on the separation efficiency, it is uncommon that a significant large pressure is applied during a CE process.

Depending on the direction of the pressure in the capillary, one can make the system into a flow counterbalanced capillary electrophoresis (FCCE) system or a pressure-assisted capillary electrophoresis (PACE) system [48], [49]. In PACE, the pressure is applied on the same direction with the direction of analyte migration. PACE can be used for accelerating migration of low-mobility molecules [50], [51], assisting bulk flow in a non-EOF separation [52] and stabilizing electrospray ionization at the CE-MS interface [41], [53].

Frontal analysis, before being used in CE, had its genesis in the field of liquid chromatography. Since reported by Kraak et.al in 1992 [44], CE-FA has been used as a technique for the characterization of non-covalent interactions between molecules [54]–[56]. Compared with other CE-based techniques, a much larger amount of sample (ca 100-150 nL) is

used in CE-FA. In analysis where biological samples (protein etc.) are analyzed, a gradually weakened EOF can be observed when an effective capillary rinsing procedure was not developed. As a result, the time of analysis will also become longer. Although increasing separating voltage could shorten the analysis time, the higher current will create a significant amount of joule heating when a BGE of higher ionic strength is used. With external hydrodynamic pressure applied during CE-FA, a much faster analysis can be achieved under a relatively low separating voltage. In CE-FA, only “front” of the plateaus instead of peaks are measured in the electropherograms, and the concentrations of ligands are determined with a pre-made calibration curve. As a result, CE-FA is not dependent on baseline resolution of the analytes, thus more tolerant to band broadening caused by the application of an external hydrodynamic pressure. Zhong et al. have demonstrated that pressure-assisted capillary electrophoresis frontal analysis (PACE-FA) is indeed capable of improving the throughput in real analysis [57]. In this work, the theoretical bases of the impact from external pressure are evaluated both mathematically and with computer simulation, and applications of PACE-FA are demonstrated.

## **2.2 Theory**

### **2.2.1 Applying external pressure to CE-FA**

In a typical set-up for CE-FA experiment, a relatively large volume (ca 100-150 nL) of the pre-equilibrated sample mixture which consists all reacting species is injected into the capillary. Once an electrical field is applied on the column, a redistribution of analytes will be caused by the differential migration of individual species. In theory, the ligand molecules that have a smaller size than the host molecules as well as the complex molecules will have a

different mobility, thus are separated under the electric field. Then the ligand plateau height is measured, and its concentration is determined with a pre-made standard calibration. By measuring the concentration of the unbound ligand molecules in a binding assay, we should be able to obtain the binding isotherm of the interactions. The correlation between the binding constants and the unbound ligand concentration at equilibria is established in the following manner.

Assuming the reaction has a 1:1 stoichiometry, the equilibrium is established as:



The binding constant  $k_1 = K$  is given by Equation 2.1, in which [H], [L] and [HL] are the concentrations of the unbound host, the unbound ligand and the complex at equilibria, respectively.

In a CE-FA binding assay, samples are prepared to contain a constant concentration of the host molecules with various ligand concentrations. As the ligand concentration increases, the number of ligand bound to per host molecule will also increase, but in a nonlinear fashion. The relationship can be described by:

$$\frac{[L]_b}{[H]_t} = \frac{k_1[L]}{1 + k_1[L]} \quad (\text{Equation 2.2})$$

where  $[L]_b$  and  $[H]_t$  are the bound ligand concentration and the total host concentration, respectively. If the concentration of unbound ligand is accurately measured, then the binding constant  $k_1$  can be obtained from a nonlinear regression of Equation 2.2.

In the conventional CE-FA experiments, the concentration of unbound ligand is determined by measuring the height of the ligand plateau. However, this approach is not accurate

when the complex has a different mobility compared to that of host molecule. Some previous works have discussed this issue [58], [59]. In a recent work, a mobility-correcting algorithm was established to expand the application range of CE-FA [54]. The relationship of the true unbound ligand concentration at equilibria with measured concentration is described by:

$$[L] = \frac{v_{HL} - v_H}{v_{HL} - v_L} [L]_t - \frac{v_L - v_H}{v_{HL} - v_L} [L]_m \quad (\text{Equation 2.3})$$

where  $[L]$ ,  $[L]_t$ ,  $[L]_m$  are the actual concentrations of unbound ligand at equilibria, total concentration of the ligand, and measured ligand concentration, respectively;  $v_{HL}$ ,  $v_H$  and  $v_L$  are the velocities of the complex, the host and the ligand molecules, respectively. By introducing the mobility terms into the equation, the overestimation of unbound ligand incurred by the dissociation of isolated complex can be eliminated. In the conventional CE-FA scenario where the host molecule is much larger in size compared to its ligand, very similar mobility of host and complex are assumed. Under this assumption, Equation 2.3 suggests that  $[L]_m$  is equal to  $[L]$ . Thus, the classic CE-FA can also be considered as a special case which fits well with Equation 2.3.

While changing the mobilities of molecules will affect the result of binding constant estimation, it is important to discuss the possible effect brought by the addition of a pressure during the CE process. In CE, the overall analyte velocity consists of three components:

$$v_A = \mu_{ep,A} E + \mu_{eof} E + v_p \quad (\text{Equation 2.4})$$

where  $v_A$  and  $v_p$  are the apparent velocity of the analyte and the additional velocity caused by pressure;  $\mu_{ep,A}$  and  $\mu_{eof}$  represent the electrophoretic mobility of the analyte and the mobility of the electroosmotic flow;  $E$  represents the electric field strength. Combining Equation 2.4 with Equation 2.3, the following equation is obtained:

$$[L] = \frac{\mu_{ep,HL} - \mu_{ep,H}}{\mu_{ep,HL} - \mu_{ep,L}} [L]_t - \frac{\mu_{ep,L} - \mu_{ep,H}}{\mu_{ep,HL} - \mu_{ep,L}} [L]_m \quad (\text{Equation 2.5})$$

It is noticed that the all terms of pressure-induced mobility are cancelled out in Equation 2.5. In other words, the measured concentration will not be affected by any non-discriminative velocity components in analyte mobility, including the pressure-driven flow and the electroosmotic flow. Given that the relative mobility of species is kept constant, speeding up the CE-FA process with external pressure should not introduce any systematic error.

### 2.2.2 Limits of applied pressure and the injected sample plug length

In a small bore open tube such as a capillary, applying pressure on incompressible liquid will create a parabolic shape of Hagen-Poiseuille flow [60]. The molecular dispersion caused by the convection can reduce the analyte concentration compared to that in the original sample plug. With other conditions unchanged, higher hydrodynamic pressure will likely cause more molecular dispersion due to stronger convection. Therefore, the measured ligand concentration might not reflect its concentration at equilibrium; then how the pressure-induced convection affects the measurements in PACE-FA needs to be understood.

If the term  $C$  is used to represent the concentration of analyte at any given spot in the capillary, the concentration being measured by the detector should be the mean value of the concentration ( $C_m$ ) over the cross section at the detect window. The mean value of the concentration can be obtained by:

$$C_m = \int_0^a (2\pi r) dr \cdot C / \pi a^2 = \frac{2}{a^2} \int_0^a Cr dr \quad (\text{Equation 2.6})$$

where  $a$  is the inner radius of the capillary and  $r$  is the distance to the center line for any given point. According to G. I. Taylor's paper published in 1953 [61], when a very thin layer of solution is being hydrodynamically injected, the plug will be distorted into a parabolic shape and its flow profile can be described by Equation 2.7:

$$x = v_0 t (1 - r^2 / a^2) \quad (\text{Equation 2.7})$$

where  $v_0$  is the maximum axial velocity of analyte and  $x$  is the distance that the analyte has migrated. While maximum velocity is found at the central line of the capillary, the analyte on the capillary wall is assumed to have a net axial velocity of zero. From Equation 2.7, the following can be derived.

$$\frac{rdr}{dx} = -\frac{a^2}{2v_0 t} \quad (\text{Equation 2.8})$$

Combining Equation 2.8 with Equation 2.6, the mean concentration is calculated as:

$$C_m = \frac{C_0 Z}{v_0 t} \quad (\text{Equation 2.9})$$

where the  $Z$  is total length of the sample plug. Equation 2.9 indicates that the analyte concentration has a constant value of  $\frac{C_0 Z}{v_0 t}$  when  $0 < x < v_0 t$ , and a value of 0 when  $x < 0$  or  $x > v_0 t$ .

In frontal analysis, a pre-equilibrated sample mixture is injected into the capillary, so that the ligand's initial concentration distribution is:

$$\begin{aligned} C &= 0, x < 0; \\ C &= C_0, 0 < x < Z; \\ C &= 0, x > Z; \end{aligned} \quad (\text{Equation 2.10})$$

As the analyte begins to migrate, a new distribution of solute is formed in the capillary.

When  $v_0t < Z$  , it can be described as:

$$\begin{aligned}
 C_m &= 0, x < 0 \\
 C_m &= C_0x / v_0t, 0 < x < v_0t \\
 C_m &= C_0, v_0t < x < Z \\
 C_m &= C_0(1 - \frac{x-Z}{v_0t}), Z < x < Z + v_0t \\
 C_m &= 0, x > Z + v_0t
 \end{aligned}
 \tag{Equation 2.10a}$$

When  $v_0t > Z$  , the distribution becomes:

$$\begin{aligned}
 C_m &= 0, x < 0 \\
 C_m &= C_0x / v_0t, 0 < x < Z \\
 C_m &= C_0Z / v_0t, Z < x < v_0t \\
 C_m &= C_0(1 - \frac{x-Z}{v_0t}), v_0t < x < Z + v_0t \\
 C_m &= 0, x > Z + v_0t
 \end{aligned}
 \tag{Equation 2.10b}$$

Thus, it is clear that the convection will broaden the sample plug. If  $v_0t > Z$  ,when the maximum displacement of the solute exceeds the total length of sample plug, the plateau height of solute is equal to  $C_0Z / v_0t$  rather than the original concentration  $C_0$  .

In order to have the measured concentration equals the original concentration,  $v_0t$  needs to be less than the total length of sample plug  $Z$  (case 10a). The migration time  $t$  can be calculated by:

$$t = \frac{L_{eff}}{v_0 + (\mu_{ep,A} + \mu_{eof})E}
 \tag{Equation 2.11}$$

Thus  $v_0t < Z$  can be written as

$$\frac{v_0}{v_0 + (\mu_{ep,A} + \mu_{eof})E} < \frac{Z}{L_{eff}} \quad (\text{Equation 2.12})$$

In Equation 2.12,  $L_{eff}$  is the length of capillary from the inlet to the detector. To calculate  $v_0$ , the Hagen - Poiseuille Equation (standard fluid-dynamics notation) is used:

$$\Delta P = \frac{8\eta L_t Q}{\pi a^4} \quad (\text{Equation 2.13})$$

where  $\Delta P$ ,  $\eta$ ,  $L_t$ ,  $Q$  and  $a$  are the pressure difference between ends of the capillary, the dynamic viscosity of the solution, the total length of the capillary, the volumetric flow rate, and the capillary inner radius, respectively.

Substitute volumetric flow rate  $Q$  with the product of capillary cross section  $\pi a^2$  and the average linear velocity  $\bar{v} = \frac{1}{2} v_0$ , Equation 2.13 becomes

$$v_0 = \frac{\Delta P a^2}{4\eta L_t} \quad (\text{Equation 2.14})$$

Combining Equations 2.13 and 2.11,

$$\frac{\Delta P a^2}{\Delta P a^2 + 4E\eta L_t(\mu_{ep,A} + \mu_{eof})} < \frac{Z}{L_{eff}} \quad (\text{Equation 2.15})$$

As mentioned above, the pressure  $\Delta P$  should always satisfy Equation 2.15. However, this mathematical equation represents the condition where only convection is considered. In real situations, diffusion also affects the distribution of solute in the capillary. When convection and diffusion are both considered, the complete solution of Equation 2.16 is required to determine solute concentration in the capillary.

$$D\left(\frac{\partial^2 C}{\partial r^2} + \frac{\partial C}{r\partial r} + \frac{\partial^2 C}{\partial x^2}\right) = \frac{\partial C}{\partial t} + v_0\left(1 - \frac{r^2}{a^2}\right) \frac{\partial C}{\partial x} \quad (\text{Equation 2.16})$$

According to Taylor's paper, the effect of diffusion can be considered separately. Radial diffusion, compared to the longitudinal diffusion, has a more significant effect on the distribution of solutes. Under radial diffusion, solute molecules near the wall are able migrate with the bulk plug. As a result, the dispersion of solute is alleviated by the molecular diffusion [61]. Without considering the diffusion, Equation 2.15 implied a more aggressive hypothesis. Thus, any value of  $\Delta P$  which satisfies Equation 2.15 should be applicable in the practical experiments.

## **2.3 Materials and methods**

### **2.3.1 Chemicals and sample preparation**

In the small molecule and cyclodextrin binding experiments, the 20 mM borate buffer was made from Borax ( $Na_2B_4O_7 \cdot 10H_2O$ ) (LingFeng Chemical Reagent Co.Ltd, Shanghai, China) with its pH adjusted to 9.1. Hydroxypropyl  $\beta$ -cyclodextrin (HP- $\beta$ -CD) was purchased from J&K Chemical Co.Ltd (Shanghai, China), para-nitrophenol and benzoic acid were purchased from Tauto Biotech Co.Ltd (Shanghai, China). In the CE-FA experiments, the HP- $\beta$ -CD was diluted to 20 mM with borate buffer. The benzoate and para-nitrophenol were made into a series of solutions with concentrations of 50  $\mu$ M, 100  $\mu$ M, 150  $\mu$ M, 200  $\mu$ M, 250  $\mu$ M, 400  $\mu$ M and 500 $\mu$ M.

### **2.3.2 Instrumentation**

All CE-FA experiments were performed on a PA800 Plus<sup>TM</sup> capillary electrophoresis system (Sciex, Framingham, MA) equipped with a photodiode array (PDA) detector. A 50 cm bare fused silica (BFS) capillary (Polymicro Technologies, Phoenix, AZ) with 50  $\mu$ m ID and 360  $\mu$ m OD was used. During frontal analysis, hydrodynamic injections were performed at 1 psi for

90 s, and the injecting volume was estimated to be 100 nL. All CE-FA runs were performed under a voltage of 15 kV, and hydrodynamic pressure of 1 psi to ensure faster analyses of all interactions.

### **2.3.3 Simulation**

A series of computational-fluid dynamics (CFD) simulations were carried out with COMSOL Multiphysics® Version 5.3 (COMSOL, Inc., Palo Alto, CA). A cylindrical tube (50  $\mu\text{m}$  i.d. and 2 cm length) was modeled in the program, and the parameters has been optimized for better meshing and higher simulation efficiency. In these numerical studies, modules of Laminar Flow and Transport of Diluted Species were used. The channel was filled with a certain percentage of the sample solution (whose diffusion coefficient is  $10^{-9} \text{ m}^2 / \text{s}$ ) initially, and the rest of channel was filled with the blank solvent. When the simulation started, an incompressible laminar fluid (blank solvent) was continually pushed into the channel through the channel inlet with a defined pressure. The boundary conditions of the inside wall were set as no slips. The concentrations of the solute at the channel outlet were recorded.

## **2.4 Results and discussion**

### **2.4.1 COMSOL Multiphysics® simulation**

Because it is difficult to find a complete analytical solution for Equation 2.16, simulation with COMSOL Multiphysics® herein is used to estimate the possible effect brought by external hydrodynamic pressure. In Figure 2.1, the plateaus produced by the simulations with different external pressure are plotted.

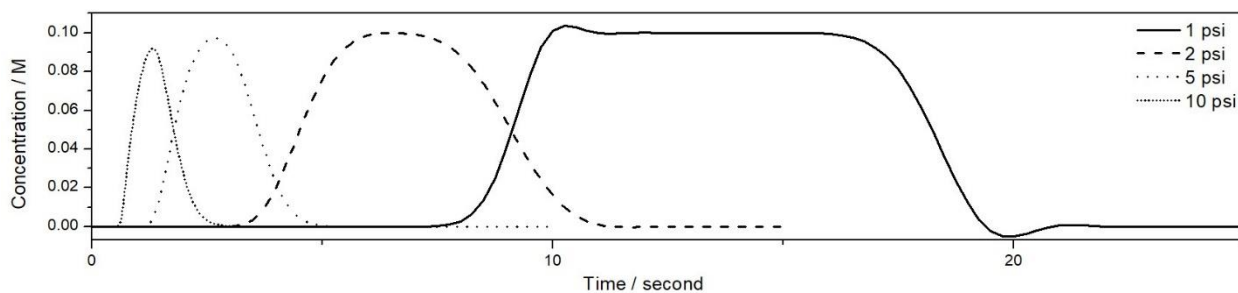


**Figure 2.1 Numerical results of the solute concentration distribution in the channel with different external pressures applied at the inlet.**

Since the solute molecules migrate faster under higher pressure, it takes less time for the sample plug to pass by the detector. Thus, as shown in Figure 2.1, the time domain plateau becomes narrower when simulated with higher pressures. Within the tested pressure of 1 - 10 psi per 50 cm capillary, nearly rectangular shape of the plateaus was observed under lower pressure (1-2 psi), and the plateaus became peaks when the pressure was higher (over 5 psi). At lower pressure inputs, no significant decrease of the plateau height was observed, and the original sample concentration is maintained. If the pressure increases, stronger convection may eventually outweigh the diffusion effect; then the plateau height is reduced which may cause inaccurate measurement. This effect becomes significant when the pressure reaches 10 psi, which makes the detected sample concentration reduces to around 90% of the original concentration. However, such a high-pressure setting might make the plateau too narrow to be measured accurately.

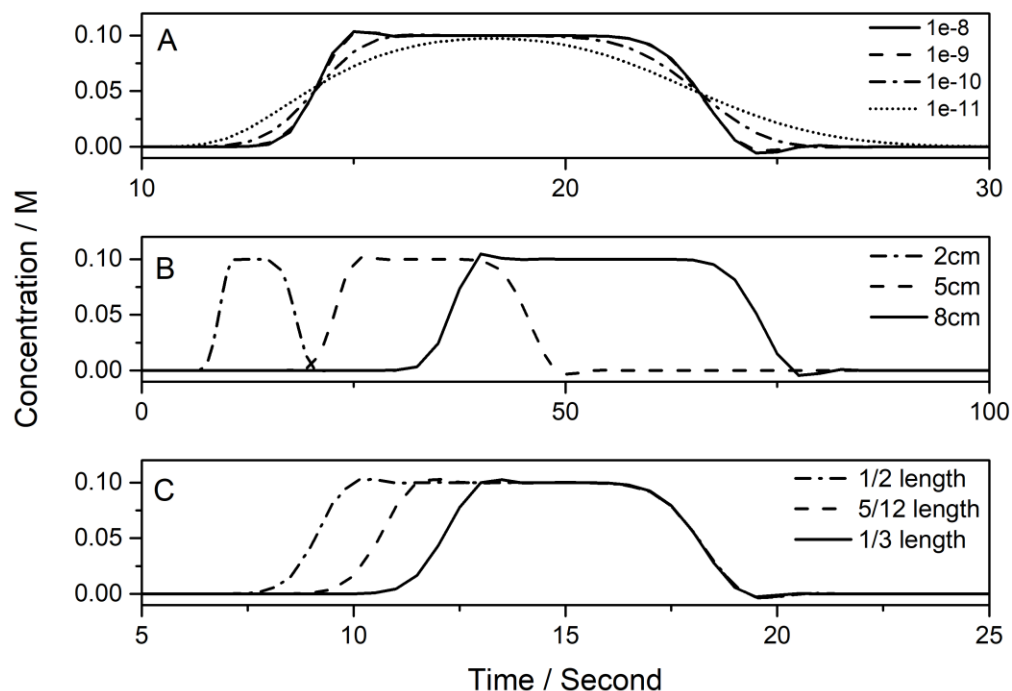


**Figure 2.2 Numerical results of the solute concentration in the channel with (A) different solute diffusion coefficient; (B) different total channel length for particles with a diffusion coefficient of  $10^{-9} \text{m}^2/\text{s}$ ; (C) different sample plug length to channel length ratio with particles used in (B). All simulations were performed under 1 psi per 50 cm capillary length, the same as what was used in the real experiment.**

To have a better understanding of factors that could potentially affect the ligand plateau height in PACE-FA, we also studied a few other parameters in the simulations. In Figure 2.2A, solutes with different diffusion coefficient (ranging from  $10^{-8} \text{m}^2/\text{s}$  to  $10^{-11} \text{m}^2/\text{s}$ ) were tested. It was observed that the plateau profile did not change much until the molecular diffusion coefficient was reduced to  $10^{-11} \text{m}^2/\text{s}$ . Since most ligand molecules have diffusion coefficient around  $10^{-9} \text{m}^2/\text{s}$ , PACE-FA should still be applicable in most situations. In addition to diffusion, the effects from the channel length and the sample plug to channel length ratio were also studied. In simulations with different channel length, the external pressure was adjusted so

that the maximum axial velocity of solute was kept the same. The plateau height is found to be almost unchanged with longer channel length (Figure 2.2B), and this can be observed as well with a different sample/blank solvent ratio in the channel (Figure 2.2C). Inferring from the simulation results, PACE-FA is adaptable to a wide range of external pressures. In addition, a small change of the measured ligand concentration is expected when some properties of the analytes (molecular diffusion coefficients, capillary length, the sample plug to channel length ratio) are changed in PACE-FA.

#### 2.4.2 Using PACE-FA to achieve faster and equally accurate analysis

In many CE applications, the EOF can be a driven force on all species. The migration time  $t$  for any of the species, is determined by the following equation:

$$t = \frac{L_{eff}}{\mu_{eof} + \mu_e} \quad (\text{Equation 2.17})$$

where  $L_{eff}$  represents the length of capillary from the sample inlet to the detector window,  $\mu_{eof}$  and  $\mu_e$  are the EOF mobility, and the electrophoretic mobility of the analyte, respectively. For molecules migrating in the electric field against the direction of EOF, the term  $\mu_e$  in Equation 2.17 may turn to be negative. If the  $\mu_{eof}$  and  $\mu_e$  have opposite signs and close absolute values, then the denominator of Equation 2.17 will be very small, and the analyte will take a long time to migrate.

In Figure 2.3, a comparison of electropherograms from CE-FA with and without a pressure is depicted. The HP- $\beta$ -CD, which has no UV absorption, can be seen as the negative plateau in both traces of the electropherograms. The benzoate carries negative charge in the basic buffer solution (pH=9.1) and is detected as the positive plateau. The plateau of benzoate has

twice the width compared to the plateau of HP- $\beta$ -CD, and it also shows two slightly different plateau heights. The left half of the plateau represents ligand dissociated from the complex during the separation, and the right half of the plateau represents the unbound ligand in the initial equilibrium.

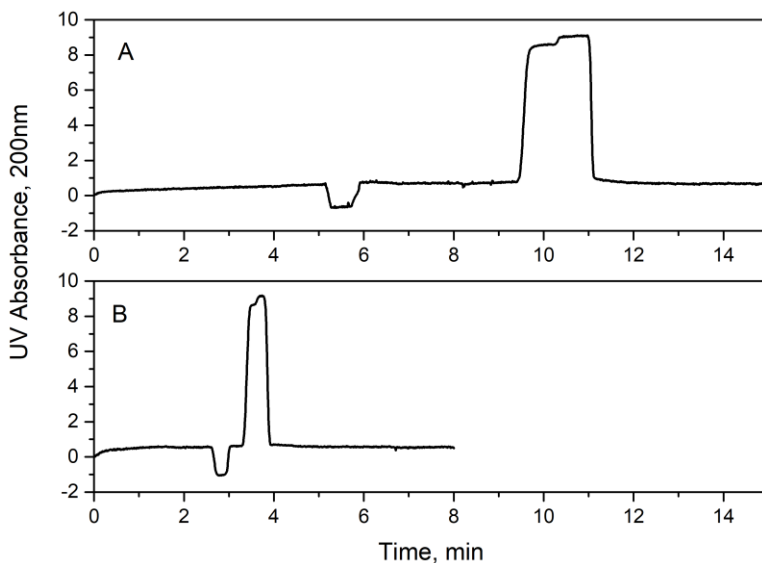


**Figure 2.3 CE-FA electropherogram of HP- $\beta$ -CD and benzoate interaction. (A) Analyzed under 15 kV; (B) Analyzed under 15 kV with 1psi pressure applied on the inlet side**

With 1 psi external pressure applied to the inlet, the migration time of benzoate changed from 9.4 ~ 11.1 min (Figure 2.3A) to 3.3 ~ 3.9 min (Figure 2.3B). The total analysis time with 1 psi per 50 cm pressure is found to be shortened to around 1/3 compared to when no pressure was used, while the plateau profile (shape, height etc.) was not significantly changed.

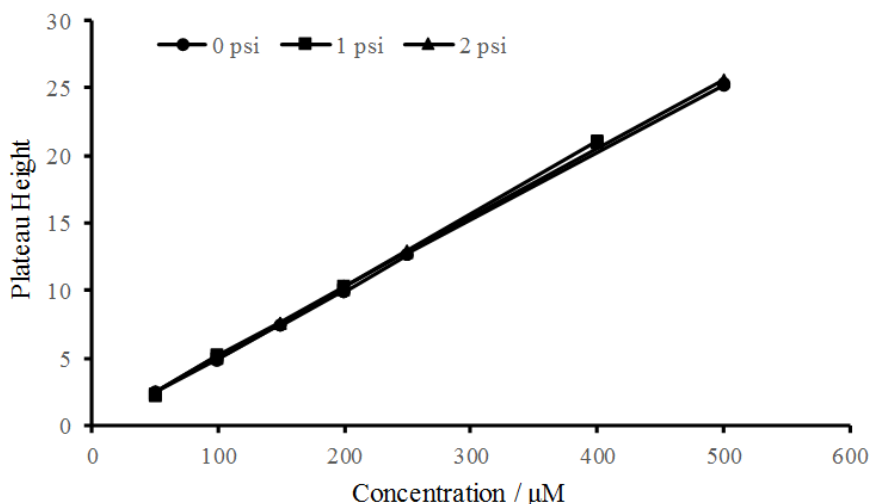


**Figure 2.4** The standard calibration curves of benzoate obtained under 0 psi+15 kV, 1 psi+15 kV and 2 psi+15 kV.

To further investigate if an external pressure in CE-FA affects the measured analyte concentration, the standard calibration curves of benzoate obtained with and without external pressure was also compared. As Figure 2.4 has shown, the curves almost completely overlap with each other. This result has provided an experimental proof to what has shown in the COMSOL Multiphysics® simulation: a pressure higher than 1 psi per 50 cm can be applied to the CE-FA system without altering the results. As long as the plateau shape is maintained, further improvement on the analysis speed can be achieved by involving a higher pressure in PACE-FA.

In the theoretical section, it has been proved that the determined binding constant will not be affected with the use of a small pressure. In order to verify it through experiments, two pairs of interacting molecules were studied with both conventional CE-FA and PACE-FA. The comparisons of binding isotherm are plotted in Figure 2.5, and the binding results are listed in Table 2.1.

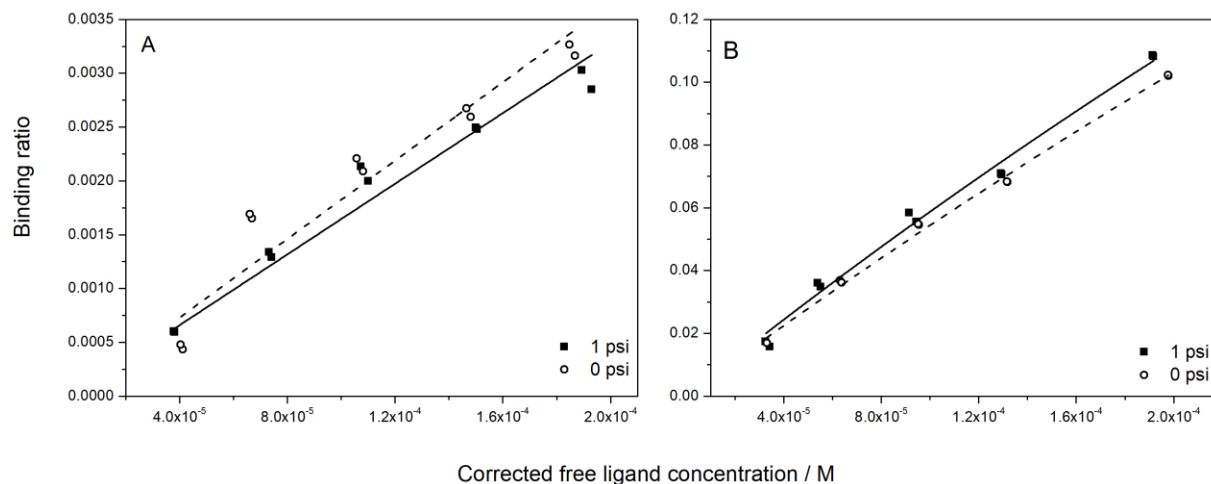


**Figure 2.5 Comparison of binding isotherms determined with CE-FA and PACE-FA. (A) HP- $\beta$ -CD with benzoate; (B) HP- $\beta$ -CD with para-nitrophenol.**

All data points plotted in Figure 2.5 have already been processed with the mobility-correction algorithm. The data points obtained without external pressure are depicted with hollow circles (regressed with dashed line) and those obtained with 1 psi external pressure are depicted with solid squares (regressed with solid line). Despite a few points showing minor differences, most of the data points measured with and without pressure are found to be very close. After analyzing with nonlinear regression, we found no significant upward/downward bias in the binding constants when an external pressure was used. More details on how the errors on binding constants can be evaluated can be found in previous publications [62], [63].

Molecular pair	CE-FA	PACE-FA	Difference in %
HP- $\beta$ -CD/para-nitrophenol	575.6 $\pm$ 6.2	623.7 $\pm$ 11.2	7.71%
HP- $\beta$ -CD/benzoate	18.3 $\pm$ 0.8	16.5 $\pm$ 0.5	9.84%

**Table 2.1 The comparison of binding constants determined from CE-FA/PACE-FA**

### **2.4.3 Using PACE-FA to analyze the interaction between molecular species with opposite charges in a neutral-coated capillary**

While CE-FA is often used to determine the affinity of non-covalent interactions between neutral and charged compounds or compounds with the same charges, it can also be used to study molecular interactions between compounds of opposite charges. However, the adsorption of the interacting species on the capillary wall has been identified as a major concern [64]. To overcome this problem, CE-FA in capillary with a neutral coating has been developed [65]. Since there is a very weak or none existing EOF in a neutral coated capillary, it is impossible to let all interacting species migrate with only an electrical potential applied to the capillary. With conventional CE-FA, only part of the species can be detected and analyzed. With PACE-FA, however, all analytes can be detected.

The practical applications of PACE-FA in the analysis of interactions between oppositely charged species has been demonstrated in another work [66]. The B cell lymphoma 2 (Bcl-2) promoter DNA quadruplex and palmatine hydrochloride interaction was characterized. With the BGE used (25 mM ammonium acetate, pH = 8), the DNA quadruplex carries multiple negative

charges while the palmatine is positively charged. All of the species were detected within 6 minutes under 1 psi pressure and 15 kV voltage in a 50 cm capillary. The positively charged small molecule ligand (palmatine) migrated first, followed by the formed complex, and then the negatively charged DNA quadruplex. With PACE-FA, a more complete set of information are provided with the electropherogram. The ligand height can be used for the binding constant calculation, and other part of the electropherogram also provides the information to conduct further kinetics and thermodynamics studies [66].

## **2.5 Conclusion**

In this work, an in-depth discussion on the PACE-FA technique is presented. The computer simulation results showed that this technique is adaptable to a relative wide range of external pressure (0-5 psi per 50-cm capillary). The experimental verification with HP- $\beta$ -CD and benzoate/para-nitrophenol has demonstrated that PACE-FA not only significantly reduces the analysis time, but also is theoretically sound and maintains the level of accuracy that is comparable to those obtained by other methods. This technique is applicable to most small molecules, as well as those larger biological molecules with bioactive conformations that require the presence of other co-factors. With similar applicability, PACE-FA brings significant improvements to the conventional CE-FA technique. In the near future, PACE-FA could potentially become a more common tool for the analysis of bio-molecular interactions.

## Chapter 3: 2D-EFD Design and Simulation Result

### 3.1 EFD desalination design

EFD devices utilize both electric field (discriminative) and hydrodynamic pressure (non-discriminative) as driving forces for fluid/analyte flow, providing better control of the analyte movement for continuous chemical purification. Herein, the objective is to develop a three-channel desalting chip. The schematic model is drawn in Figure 3.1 below.

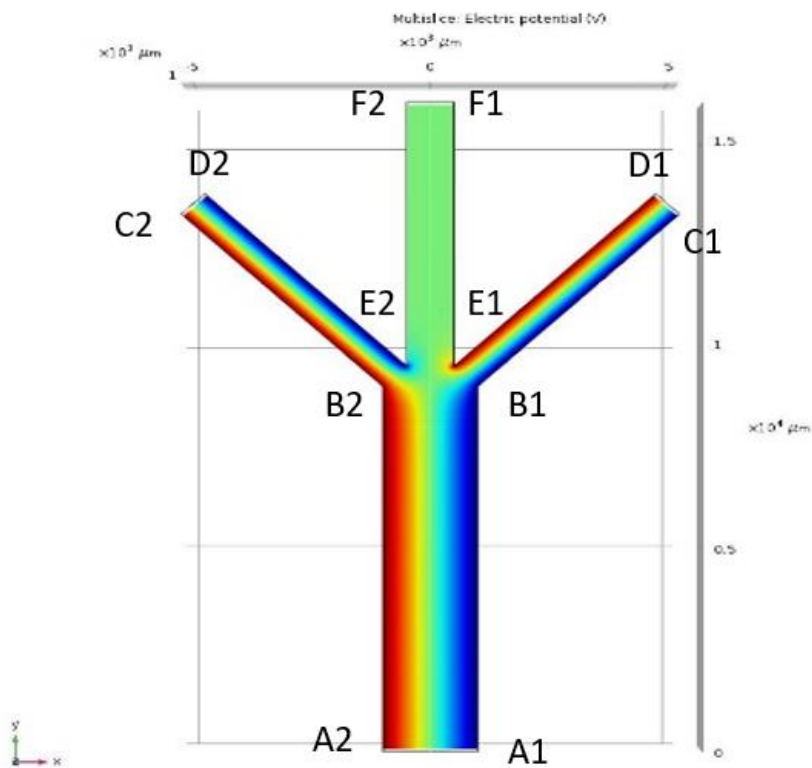
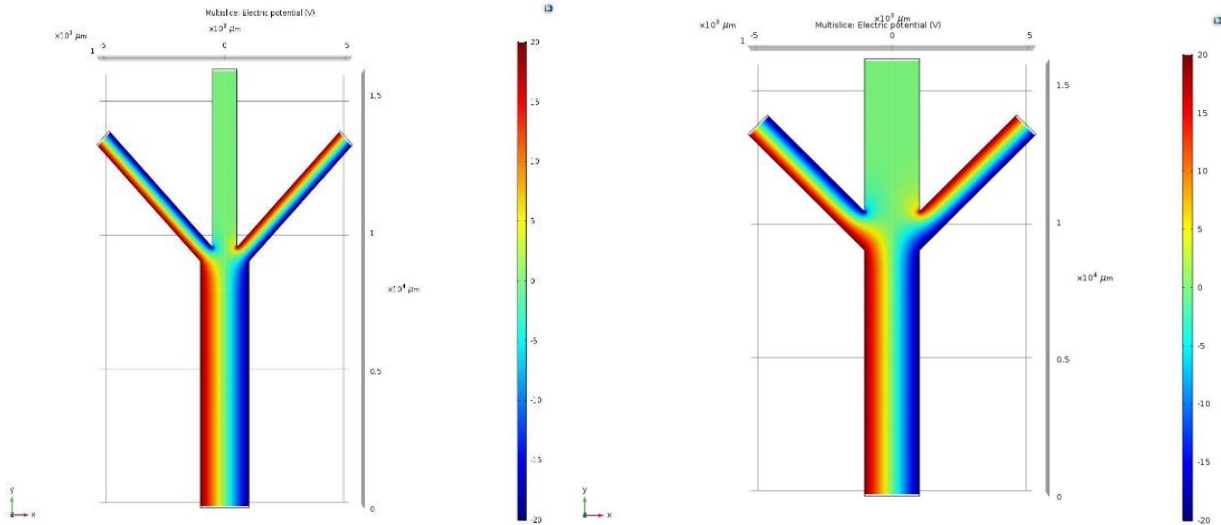


Figure 3.1 Schematic drawing of the geometry of the EFD desalination design (on the x-y plane). The electrodes are placed at A1B1, B1C1, D1E1, A2B2, B2C2 and D2E2 respectively.

Regarding the geometry of this 2D-EFD device, there are two geometries of interest which are used in this study: Type 1 and Type 2, where the only difference is that the main

channel width (F1F2) equals the injection channel (A1A2) width in the Type 2 design but not in the Type 1 design.



**Figure 3.2 Different geometry of the EFD desalination design: Type 1 (on the left) vs Type 2 (on the right).**

### 3.1.1 2D-EFD working principle and workflow of the simulation

The simplified Navier-Stokes equation in vector form is:

$$\rho \frac{\partial \overrightarrow{v}_{particle}}{\partial t} + \rho (\overrightarrow{v}_{particle} \cdot \nabla) \overrightarrow{v}_{particle} = \rho \overrightarrow{g} - \nabla p + \eta \nabla^2 \overrightarrow{v}_{particle} \quad (\text{Equation 3.1})$$

where  $\nabla p$  represents the pressure gradient [Pa/m],  $\overrightarrow{v}_{particle}$  represents the particle velocity [ $\text{m}^2/\text{s}$ ],  $\overrightarrow{g}$  represents the gravitational acceleration [ $\text{m}^2/\text{s}$ ],  $\eta$  represents the viscosity coefficient [ $\text{m}^2/\text{s}$ ],  $\rho$  represents the density [ $\text{kg}/\text{m}^3$ ].

The flow is considered to be Stokes flow which means that the left side can be considered negligible. Furthermore, the Reynold's number in this study is around 4.48 therefore a laminar

flow can be assumed. Then, if the body force is ignored, then the following equation can be derived (which is used to solve the fluid field)

$$-\nabla p + \eta \nabla^2 \overrightarrow{v_{particle}} = 0 \quad (\text{Equation 3.2})$$

where  $\overrightarrow{v_{particle}}$  can be rewritten as  $\overrightarrow{v_f}$ , the net fluid velocity [m/s].

The conservation of mass states:

$$\frac{\partial \rho}{\partial t} + \nabla \cdot \rho \overrightarrow{v_f} = 0 \quad (\text{Equation 3.3})$$

Herein, the fluid is incompressible; the density is therefore constant, which can be used to simplify the equation above to:

$$\nabla \cdot \overrightarrow{v_f} = 0 \quad (\text{Equation 3.4})$$

Together with the simplified Navier-Stokes equation, we can then solve for the fluid field  $\overrightarrow{v_f}$ .

The mass balance equation can be written:

$$\rho \frac{\partial c}{\partial t} + \rho \nabla \cdot (-D \nabla c) + \rho \vec{v} \cdot \nabla c = r \quad (\text{Equation 3.5})$$

where  $r$  represents the chemical reaction rate for the studied species,  $D$  represents the diffusion coefficient [ $\text{m}^2/\text{s}$ ],  $c$  represents the concentration. The  $\vec{v}$  [m/s] herein represents the sum of the all direct displacement velocities of the analyte, which includes electrophoretic velocity  $\overrightarrow{v_{ep}}$ , electro-osmotic velocity  $\overrightarrow{v_{eo}}$  and pressure-induced velocity  $\overrightarrow{v_p}$ ;  $\overrightarrow{v_f}$  is the exact net fluid velocity, which can be determined by Navier-Stokes equation.

$$\vec{v} = \overrightarrow{v_{ep}} + \overrightarrow{v_{eo}} + \overrightarrow{v_p} = \overrightarrow{v_{ep}} + \overrightarrow{v_f} \quad (\text{Equation 3.6})$$

Herein, the electrophoretic velocity can be obtained by

$$\vec{v}_{ep} = \mu_{ep} \vec{E} \quad (\text{Equation 3.7})$$

where the  $\vec{E} = -\nabla V$  represents the applied electrical field [V/m].

Therefore, if we have a system in which no chemical reaction occurs, the mass transport equation becomes

$$\frac{\partial c}{\partial t} + \nabla \cdot (-D \nabla c) + (\mu_{ep} \vec{E} + \vec{v}_f) \cdot \nabla c = 0 \quad (\text{Equation 3.8})$$

In summary, the mass transport equation has been written in terms of the fluid field  $\vec{v}_f$  and the electrical field  $\vec{E}$  from the equations above. Together with the initial and boundary conditions, the concentration profile can then be obtained.

The migration behaviors of analytes in 2D-EFD device can be modeled using finite-element-scheme software (e.g. COMSOL Multiphysics) following the workflow given in Figure 3.3. In this study, all the simulations were done using COMOSL Multiphysics 5.3a and the results are shown below.

Solving the electric field:

$$\begin{cases} \nabla^2 V = 0 \\ V = V_0 \\ \vec{n} \cdot \nabla V = 0 \end{cases} \quad \longrightarrow \quad \vec{E} = -\nabla V$$

Solving the fluid field:

$$\begin{cases} -\nabla p + \eta \nabla^2 \vec{v}_f = 0 \\ \nabla \cdot \vec{v}_f = 0 \\ \vec{v}_f = \vec{v}_0 \\ P = P_0 \\ \vec{v}_f = \mu_{eo} \vec{E} \end{cases} \quad \longrightarrow \quad \vec{v}_f$$

Solving mass balance equation:

$$\begin{cases} \frac{\partial c}{\partial t} + \nabla \cdot (-D \nabla c) + (\vec{v}_f = \mu_{ep} \vec{E}) \cdot \nabla c = 0 \\ c = c_0 \\ \vec{n} \cdot (-D \nabla c) = 0 \\ \vec{n} \cdot (-D \nabla c + \vec{v}_f c + \mu_{ep} \vec{E} c) = 0 \end{cases} \quad \longrightarrow \quad c$$

Figure 3.3 Workflow of the simulation.

### 3.1.2 Geometry, design, numerical solutions and simulation

As introduced in the previous section, the workflow of the simulation process consists of three main parts: the electric field ( $\vec{E} = -\nabla V$ ), the fluidic field ( $\vec{v}_f$ ) and the concentration ( $c$ ) which are determined by solving the mass balance equation.

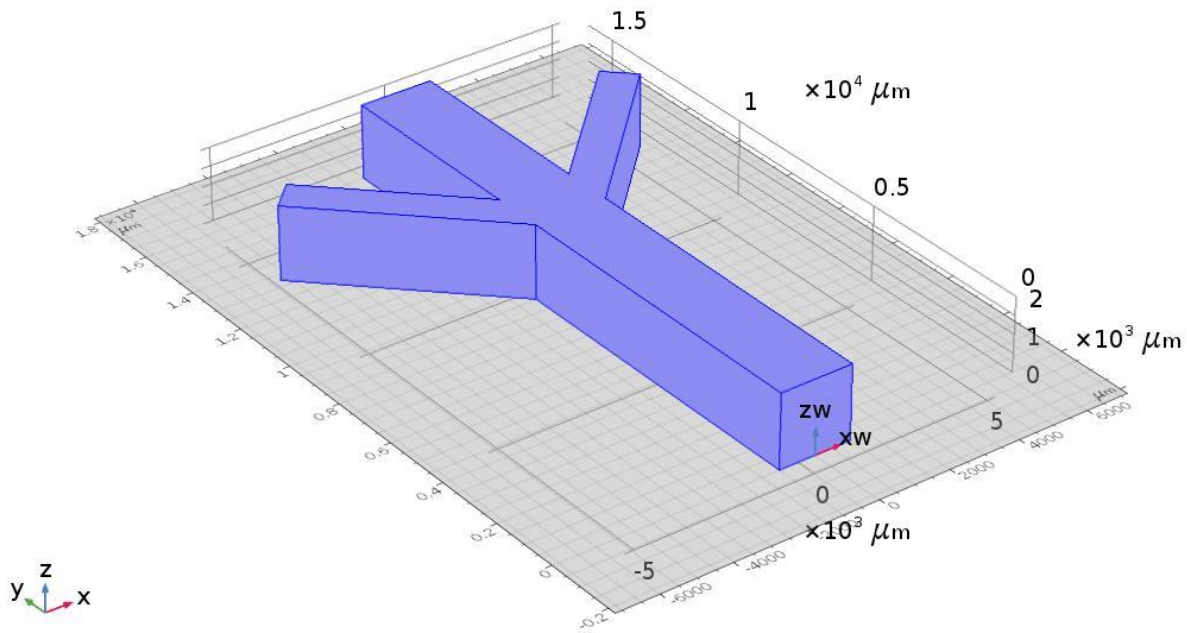


**Figure 3.4 EFD device schematic model in COMSOL. The samples flow into the surface defined by zw and xw and outflow through the three channel arms at the opposite end of the device.**

A model of the EFD device geometry (Type 2) studied is shown in Figure 3.4 above; the actual device dimensions are provided in Table 3.1. The working fluid tested is a net neutral sample of NaCl in water. There are three component concentrations that need to be studied using the model: sodium ions (one positive charge), chloride ions (one negative charge) and neutral component (water). The fluidic flow enters from the bottom port (through the injection channel) driven by an inlet pressure which provides a mean velocity of 6 cm/min (0.001 m/s) inside the injection channel (hydraulic diameter is 2 mm); the fluid components exit from the top three channels (named as “channel 1”, “channel 2”, “channel 3”, respectively). Laminar flow was assumed. There are six planar electrodes placed at the surfaces of the channel 1, channel 3 and

the injection channel, which can be used to generate the defined electric field by applying a suitable voltage to each. This EFD device was modeled as a three-channel chip with a length of 9 mm for the injection channel, a thickness of 2 mm, and a total length of 16 mm. The angle between the side exit channel (channel 1 or channel 3) and the main exit channel (channel 2) was modeled as 45 degrees.

	Type 1		Type 2
Total length (mm)	16	AF	16
Angle (degree)	45	theta(<DEF)	45
Injection width (mm)	2	A1A2	2
Main width (mm)	1	F1F2	2
Length_AB (mm)	9	AB	9
Length_BC (mm)	6	BC	6
Height (mm)	2	height	2
Width_branch (mm)	0.707	C1D1	1
	Pattern 1		Pattern 2
A1B1	Vg	A1B1	Vn
A2B2	Vp	A2B2	Vp
B1C1	Vg	B1C1	Vn
B2C2	Vp	B2C2	Vp
D1E1	Vg	D1E1	Vg
D2E2	Vp	D2E2	Vg
Vp(Volt)	20	Vp(Volt)	20
Vg(Volt)	0	Vn(Volt)	-20
		Vg(Volt)	0

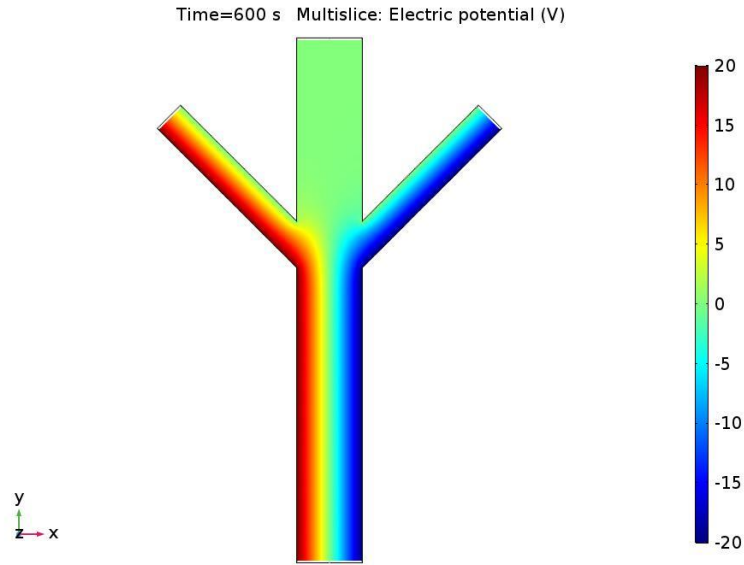
**Table 3.1 Dimensions and parameter settings for EFD desalination model.**

The available mesh options in COMSOL are categorized as different levels which are not necessarily suitable for these studies. Thus, a customized meshing option was used (set manually to mesh finer at the boundary and refine the corner) to create the grid. The maximum element size was 307  $\mu\text{m}$  and the minimum element size was 91.6  $\mu\text{m}$  (based on the default meshing options ‘Normal’ and ‘Fine’). The equations were solved under steady-state conditions for the

fluid field and the electric field with a no-slip boundary condition at the device wall and zero pressure at the outflow (to suppress backflow). The equations were solved in time-dependent mode for the mass transport part in order to observe and monitor the migration behavior. The diffusion coefficients for sodium ions ( $\text{Na}^+$ ), chloride ions ( $\text{Cl}^-$ ) and the neutral component are set to be  $1.330 \times 10^{-9} \text{ m}^2 / \text{s}$  ,  $2.030 \times 10^{-9} \text{ m}^2 / \text{s}$  ,  $1.0 \times 10^{-9} \text{ m}^2 / \text{s}$  respectively; the diffusion coefficients for copper ions ( $\text{Cu}^{2+}$ ) and sulfate ions ( $\text{SO}_4^{2-}$ ) are  $0.733 \times 10^{-9} \text{ m}^2 / \text{s}$  and  $1.070 \times 10^{-9} \text{ m}^2 / \text{s}$  ), respectively, based on the ‘Table of Diffusion Coefficients’ in [34]. The reference temperature is the room temperature ( $20 \text{ }^\circ\text{C}$ ). The initial concentration was set to 1mM for all the components. The relative tolerance for the fluidic flow field and the electric field were all set to be 0.001. Several different models were studied in the following sections, but they are essentially variations on the specific model described above.

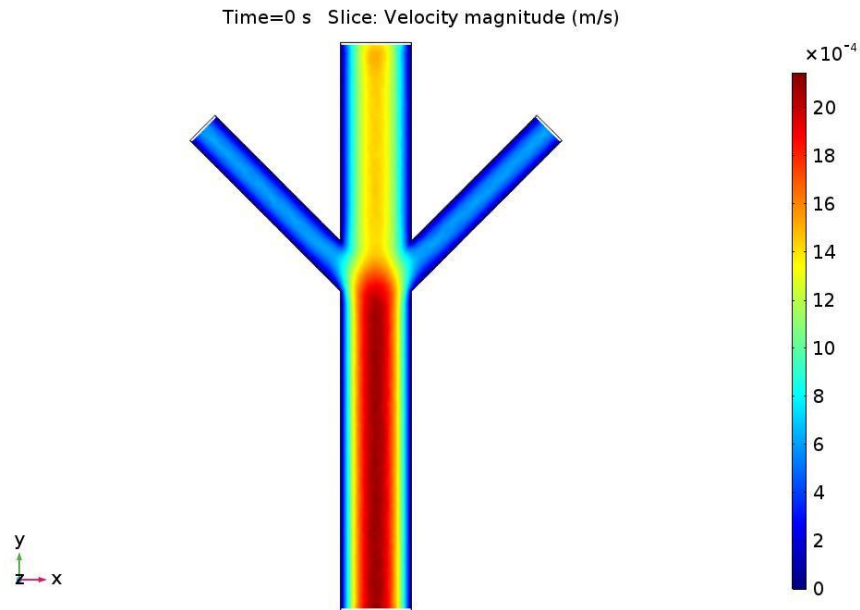
### **3.1.3 Results and discussion**

As described in the previous section, the EFD device was modeled using a net neutral sample with NaCl in water solution as the working fluid. Figure 3.5 below shows the resulting electric potential distribution based on the electric field pattern 2 in the Table 3.1 with a bi-polar input of  $\pm 20\text{V}$ .



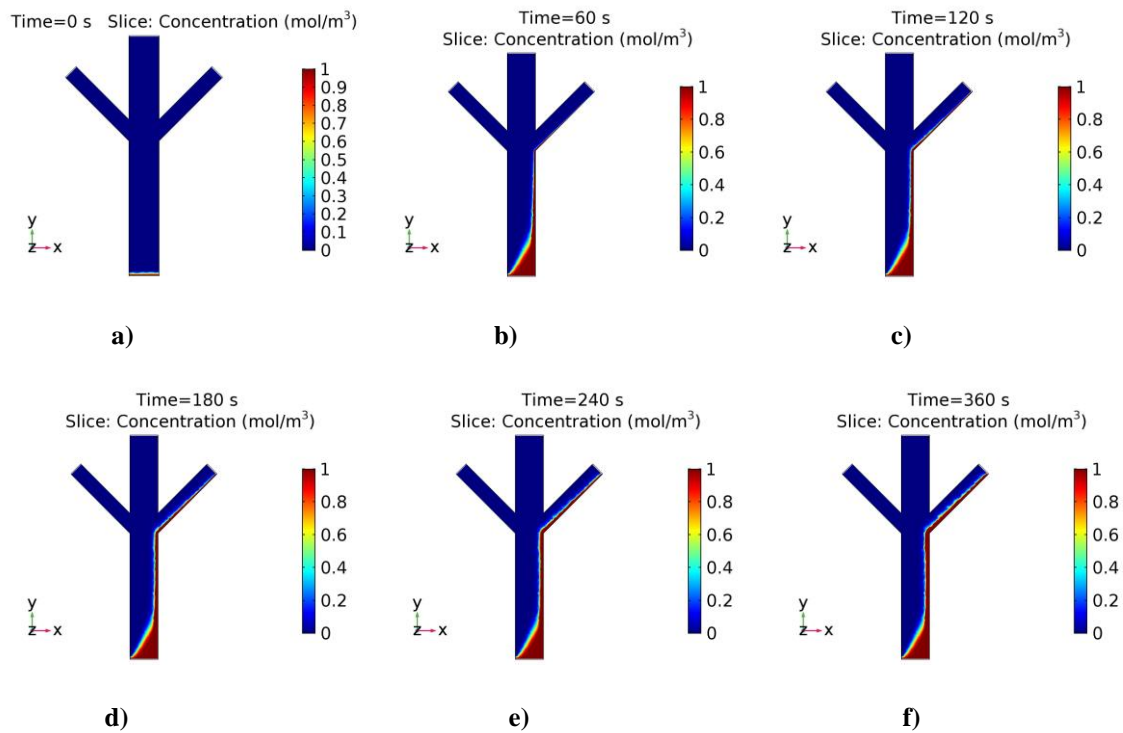
**Figure 3.5 EFD electric potential distribution for the Type 2 geometry.**

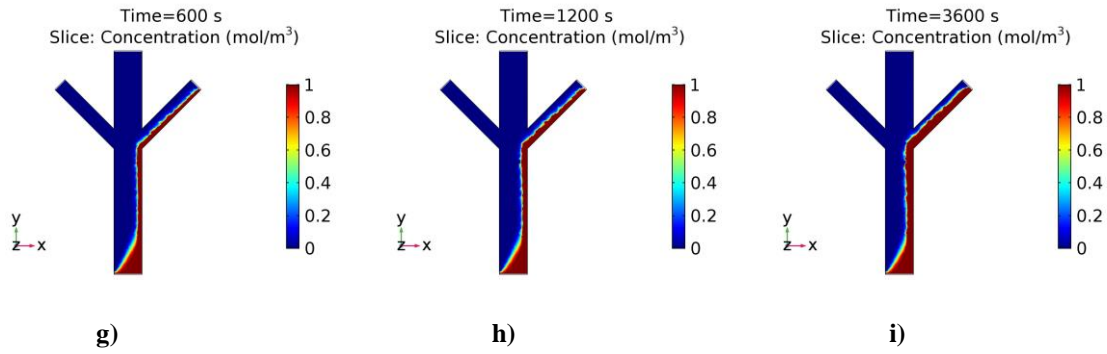
In addition to the generated electric field, the velocity distribution was modeled. As shown in Figure 3.6, the working fluid migrates relatively slower in the main exit channel (channel 2) than the injection channel (where the maximum velocity inside is around 2.5 mm/s.), but still faster than in the side exit channels (channel 1 and channel 3).



**Figure 3.6 Velocity distribution inside the EFD device (front view).**

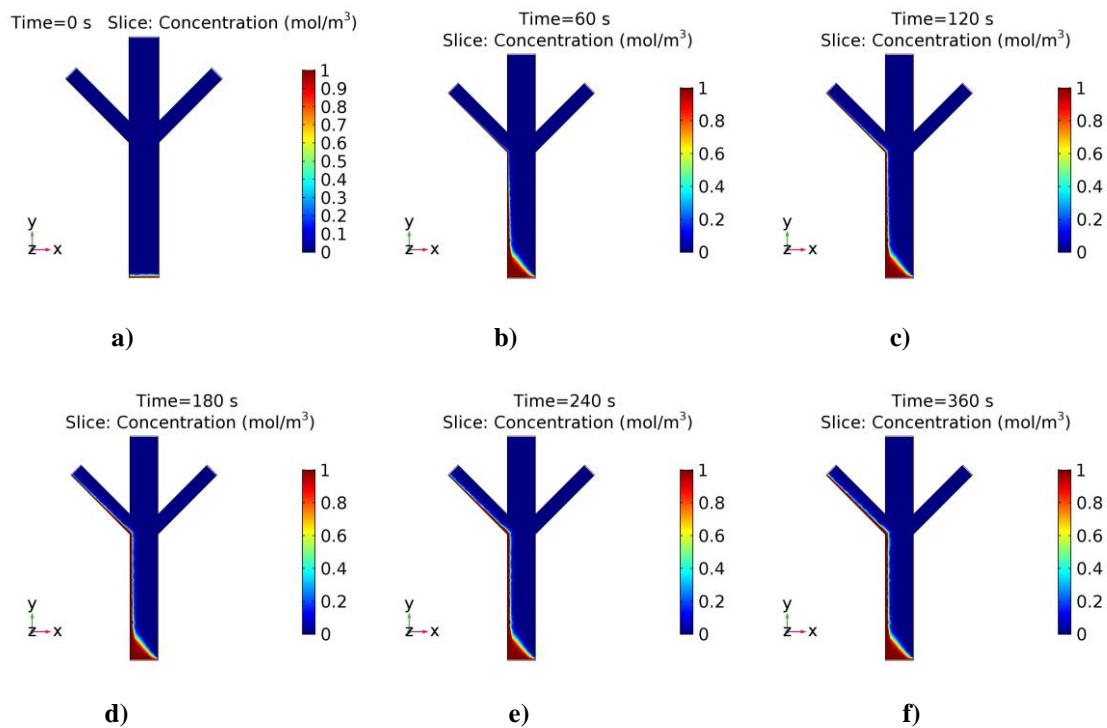
Figures 3.7-3.9 show the migration behaviors of the different components inside the device channels as a result of the hydrodynamic pressure and the generated electric field. From Figure 3.7, the sodium ions migrate towards to the right-side exit channel (channel 3) and do not outflow through the other channels, which is in good agreement with the expected results. Therefore, the EFD device ‘purifies’ the Na<sup>+</sup> ions in the analyte stream and directs the sodium ions toward the specific exit channel. Qualitatively similar behavior can also be observed for the case of the chloride ions as shown in Figure 3.8, except these negatively charged ions exit via channel 1.

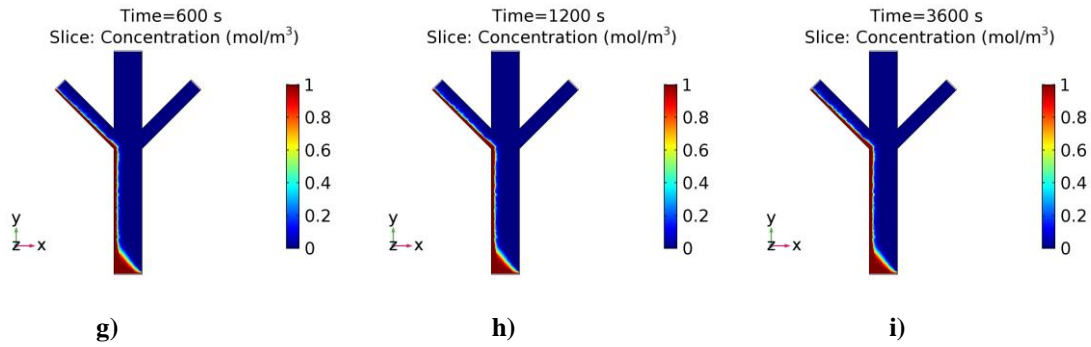




**Figure 3.7 Concentration distribution of the sodium ions inside the EFD device at different times (front view).**  
**a) time=0sec; b) time=60 sec; c) time=120 sec; d) time=180 sec; e) time=240 sec; f) time=360 sec; g) time =600 sec; h) time=1200 sec; i) time=3600 sec. The electrode voltages were  $V = \pm 20V$ .**

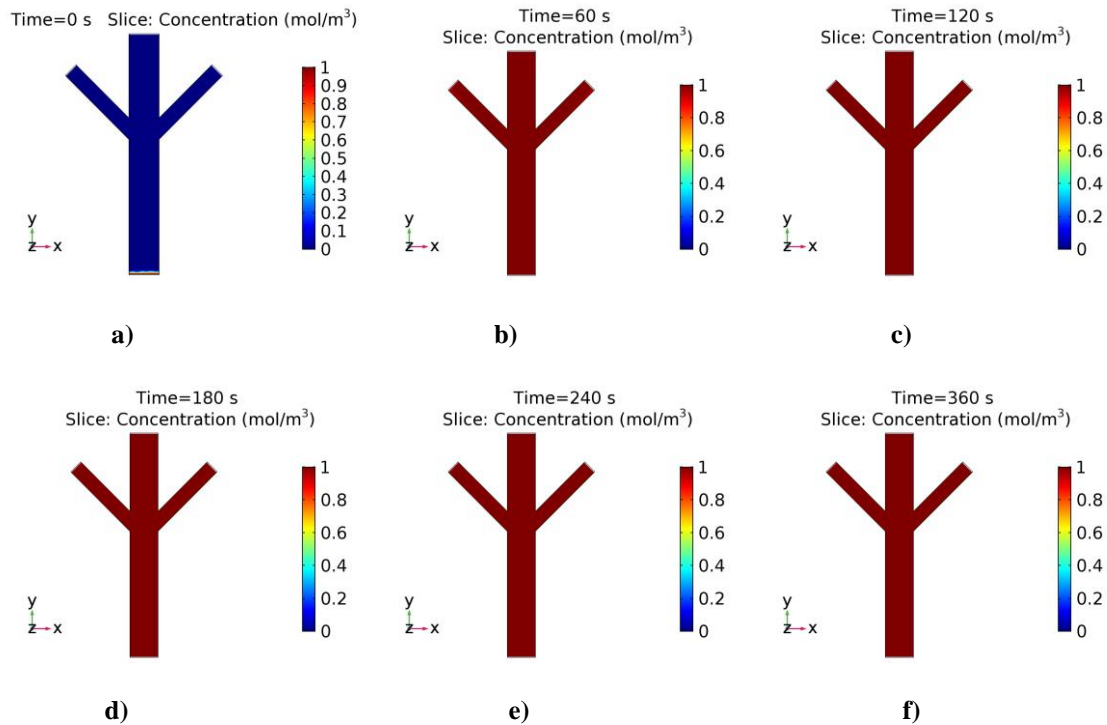
Note that the migration behaviors of the sodium ions ( $\text{Na}^+$ ) and chloride ions ( $\text{Cl}^-$ ) are not exactly the same (even though their charge numbers are the same). The reason is that their diffusion coefficients are different, so their fluxes are different even under otherwise similar conditions as expected based on Equation 1.4 or Equation 3.8.





**Figure 3.8** Concentration distribution of the chloride ions inside the EFD device at the different times (front view). a) time=0sec; b) time=60 sec; c) time=120 sec; d) time=180 sec; e) time=240 sec; f) time=360 sec; g) time=600 sec; h) time=1200 sec; i) time=3600 sec. The electrode voltages were  $V = \pm 20V$ .

Since the neutral component was not driven by the electric field, they migrate toward all of the exit channels indifferently as shown in Figure 3.9.



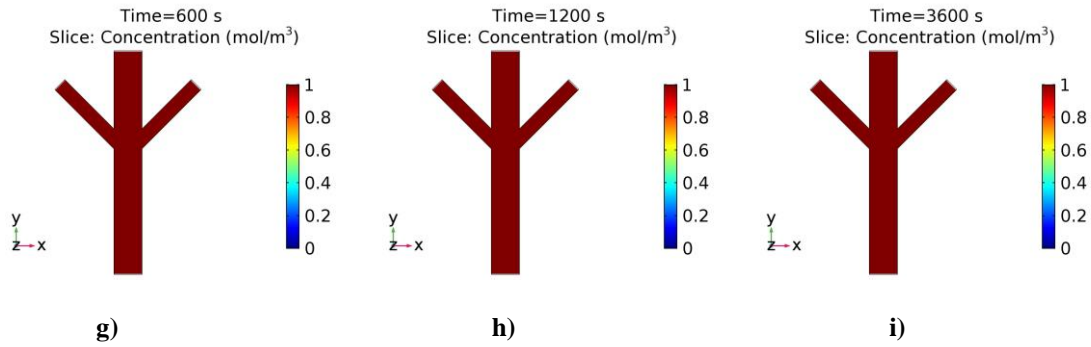
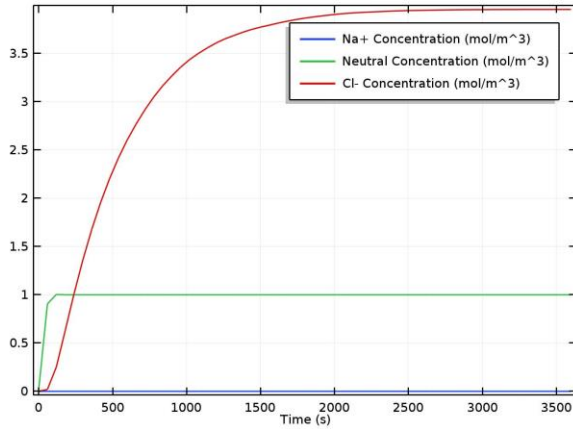
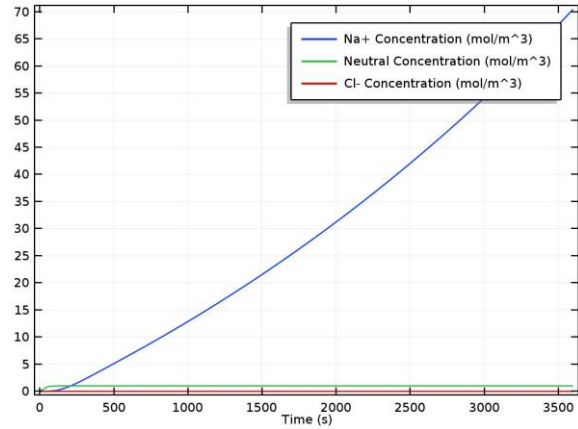


**Figure 3.9 Concentration distribution of the neutral component inside the EFD device at different times (front view). a) time=0sec; b) time=60 sec; c) time=120 sec; d) time=180 sec; e) time=240 sec; f) time=360 sec; g) time =600 sec; h) time=1200 sec; i) time=3600 sec. The electrode voltages were  $V=\pm 20V$ .**

The average concentrations at the cross-sectional surfaces at the very end of the exit channels were calculated separately and were plotted in Figure 3.10 and Figure 3.11. Figure 3.10 (a) shows that the chloride ions migrate towards to channel 1 while the sodium ions do not, as expected. The neutral component reaches a plateau quickly because its movement is not affected by the electric field. Similar results can be observed for the channel 3.



a) Left-side exit channel (channel 1)



b) Right-side exit channel (channel 3)

**Figure 3.10** Average surface concentration at the very end of the EFD device side exit channels (cross-sectional). a) left-side exit channel (channel 1); b) right-side exit channel (channel 3). The electrode voltages were  $V = \pm 20V$ .

From Figure 3.11, it can be seen that the neutral component reaches a plateau quickly within 100 sec (less than 2 min, which can also be concluded from Figure 3.9 (a-d)); there are almost no ionic components appearing in the main exit channel, which is consistent with the expectation that the analytes are desalted. Therefore, this simplified device may be able to be used for desalination.

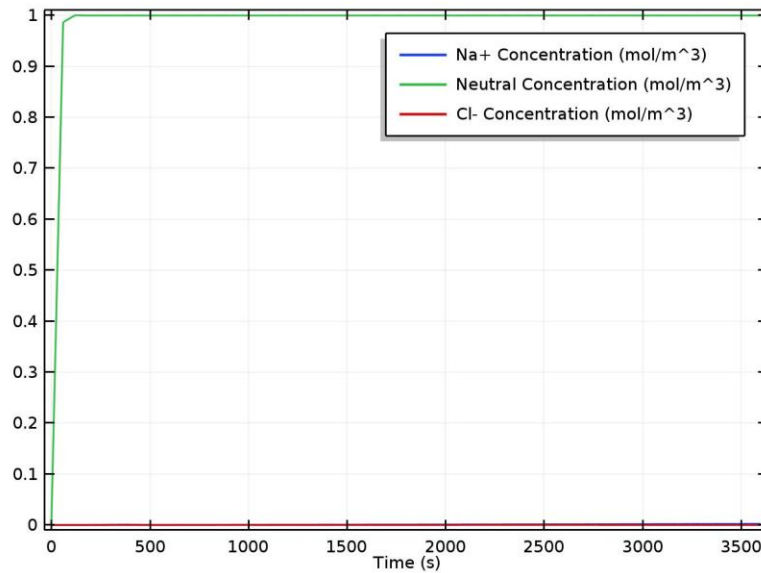


**Figure 3.11 Average surface concentration at the very end of the EFD device main exit channel (cross-sectional). The electrode voltages were  $V = \pm 20V$ .**

Based on these results, the following points are worthy of further consideration and study:

1. Electric field. With different electric potentials applied to the electrodes, the EFD desalination performance may change a lot.
2. Multi-elements in parallel. Since the ionic components migrate and outflow through the ion-specific side exit channels, there may be some potential benefit if the EFD chip device utilizes multiple single elements placed in parallel.
3. Injection channel width. Width is also worthwhile to be investigated as there may be advantages in terms of the ion trajectories, although the effective electric field within the channel will be affected.
4. Injection channel length. From Figure 3.7(i), it can be inferred that the side exit channel may become filled with ionic component after several hours); the amount of the ionic

component in each of the side exit channels might be reduced by adjusting the injection channel length.

### 3.2 EFD desalination design vs electric potential

#### 3.2.1 Geometry, design, numerical solutions and simulation

The model introduced above will be explored in more detail by varying the bi-polar voltage applied to the electrodes from  $\pm 10V$  to  $\pm 30V$ ; all of the other parameters and conditions will be kept unchanged (as listed in Table 3.2). The working fluid tested is still the net neutral sample with NaCl in water solution.

	Type 2	
Total length (mm)	16	AF
Angle (degree)	45	theta(<DEF)
Injection width (mm)	2	A1A2
Main width (mm)	2	F1F2
Length_AB (mm)	9	AB
Length_BC (mm)	6	BC
Height (mm)	2	height
Width_branch (mm)	1	C1D1
	Pattern 2	
A1B1	Vn	
A2B2	Vp	
B1C1	Vn	
B2C2	Vp	
D1E1	Vg	
D2E2	Vg	
Vp(Volt)	10,15,20,25,30	
Vn(Volt)	-10,-15,-20,-25,-30	
Vg(Volt)	0	

**Table 3.2 Dimensions and parameter settings for EFD desalination model. The changes compared to Table 3.1 are highlighted in green.**

### 3.2.2 Results and discussion

The average component concentrations at the cross-sectional surface at the very end of the exit channels were plotted separately in Figures 3.12 to 3.14.

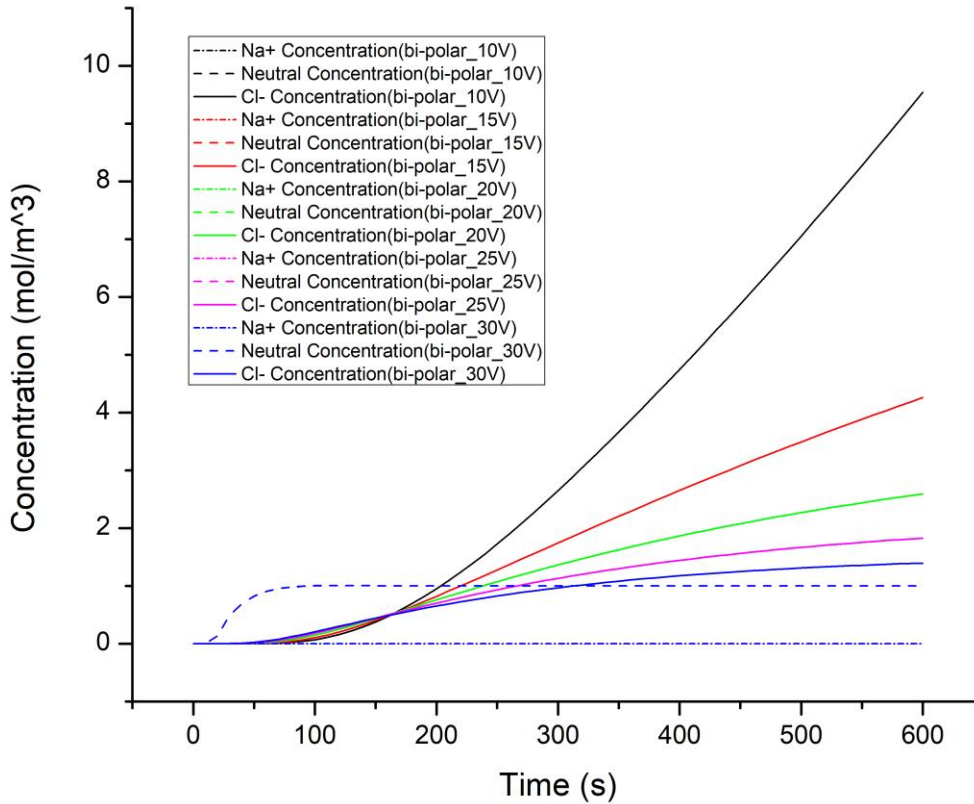


Figure 3.12 Average concentrations at the very end of the side exit channel 1 (cross-sectional) based on different electric potentials applied to the electrodes. The electrode voltages were  $V = \pm 10V, \pm 15V, \pm 20V, \pm 25V$  and  $\pm 30V$ .

Figure 3.12 shows that the chloride ions (solid lines) in all cases migrate towards channel 1 while the sodium ions do not (short dash lines), as expected. The neutral component reaches a plateau quickly in all cases; the individual lines are overlapped so that only the blue dashed line

displays. With a stronger generated electric field, the effect due to the non-diffusional (e.g. electric field) velocities becomes stronger. This can be explained by the minus sign in Equation 3.9 (re-stated from the Equation 1.3) which leads to a smaller time concentration profile. From Figure 3.12, it can be observed that  $\frac{\partial c}{\partial t}$  for the case with electrode voltages  $\pm 30V$  is less than the one for  $\pm 10V$ .

$$\frac{\partial c}{\partial t} = -(U + v) \frac{\partial c}{\partial z} + D \frac{\partial^2 c}{\partial z^2} = -W \frac{\partial c}{\partial z} + D \frac{\partial^2 c}{\partial z^2} \quad (\text{Equation 3.9})$$

where  $W$  symbolizes the total of all non-diffusional displacement velocities.

Moreover, regarding the intersection with the neutral component plateau, it takes less time for the chloride ions to migrate to channel 1 for the case where the electrode voltages are  $\pm 10V$  than for the case  $\pm 30V$ . The stronger electric field strength ( $\vec{E} = -\nabla V$ ) causes the ionic components to be pulled stronger toward the electrodes along the injection channel and therefore the intersection point appears later.

For all the cases, in order to satisfy the law of conservation of mass (i.e., for any system closed to all transfers of matter and energy, the mass of the system must remain constant over time), the ultimate state would be reached where the ionic component concentration profile will exhibit saturation. This effect is consistent with the results displayed in the figures except for the case where the voltage is  $\pm 10V$  as the simulation is terminated before the plateau is evident.

Similarly, Figure 3.13 shows the average concentration over the cross-sectional area at the end of channel 3. The sodium ions in all cases migrate to channel 3, as expected. However, the concentration profile behaviors of the sodium ions ( $Na^+$ ) and chloride ions ( $Cl^-$ ) are not the same (even though their charge number are the same). The reason is that their diffusion

coefficients are different, as noted earlier in section 3.1.3 and as expected based on Equation (1.4) or Equation (3.8).

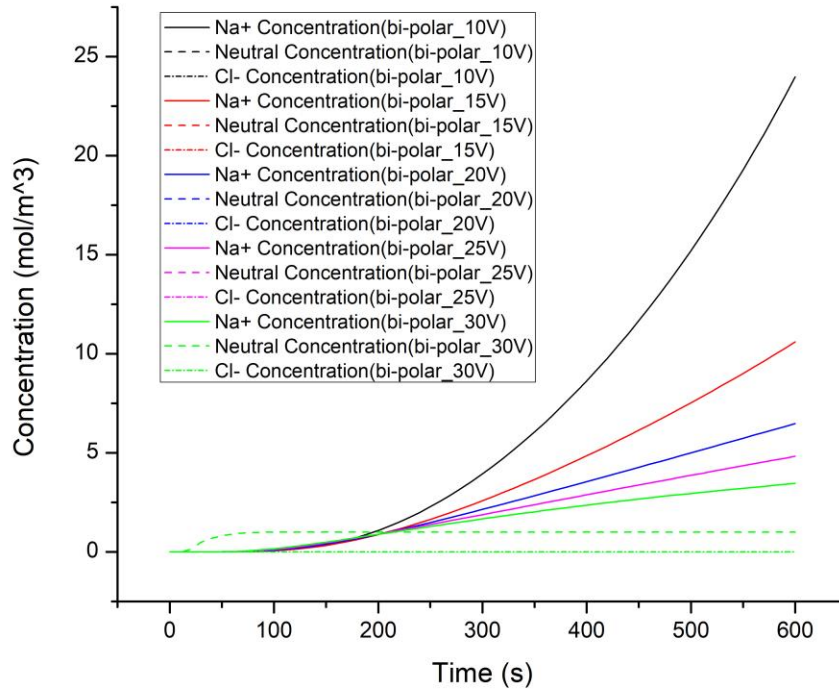


**Figure 3.13** Average concentrations at the very end of the side exit channel 3 (cross-sectional) based on different electric potentials applied to the electrodes. The electrode voltages were from  $V = \pm 10V, \pm 15V, \pm 20V, \pm 25V$  and  $\pm 30V$ .

Figure 3.14 shows the migration behaviors of the three components in the main exit channel (channel 2). All the neutral component lines are overlapped, and all the other component lines are nearly zero, which means that there are no ionic components that outflow from this channel. This result agrees with the expectation that the analytes are desalted.

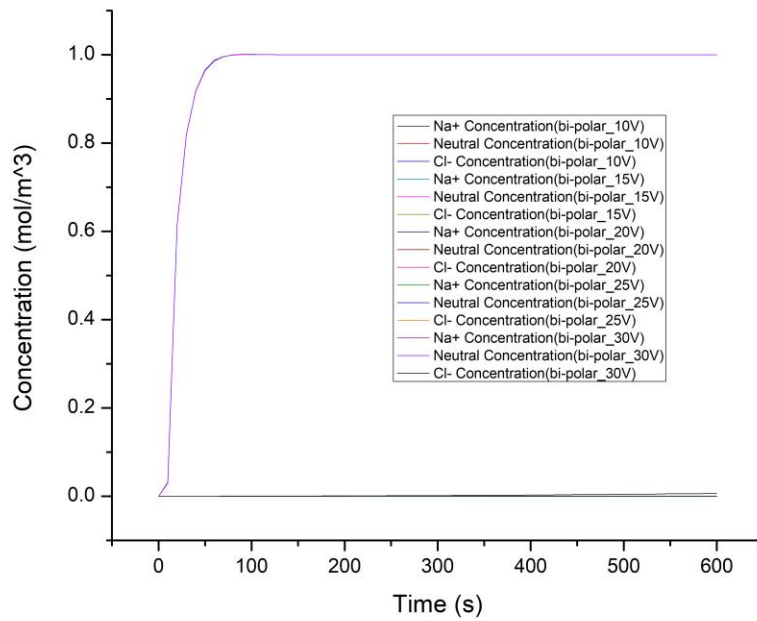


**Figure 3.14** Average concentrations at the very end of the main exit channel 2 (cross-sectional) based on different electric potentials applied to the electrodes. The electrode voltages were  $V = \pm 10V, \pm 15V, \pm 20V, \pm 25V$  and  $\pm 30V$ .

### 3.3 Multi-element EFD in parallel vs electric potential

#### 3.3.1 Introduction

It has been shown that the basic desalination process could be achieved using a single device of the design considered in sections 3.1 and 3.2. Hence, it is reasonable to suppose that overall performance could be improved if multiple elements are combined in parallel and/or in series. Herein, three elements placed in parallel are studied. The geometry of the model is shown in Figure 3.15; the dimension and parameter settings are listed in Table 3.3 below.

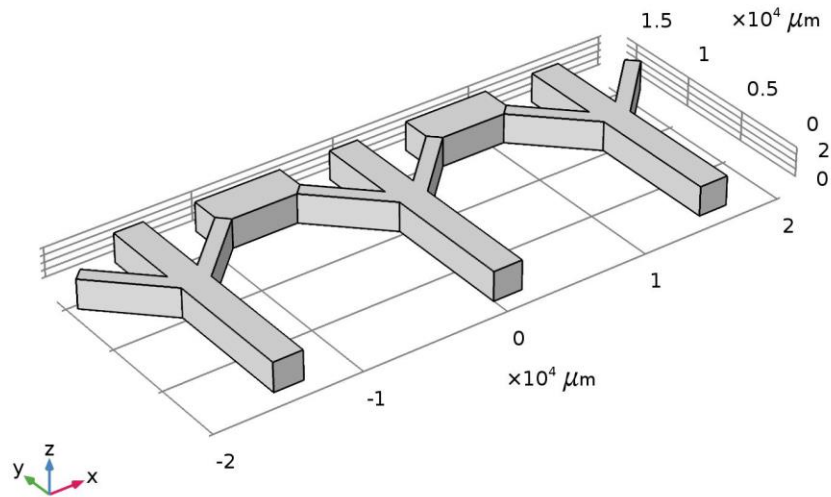


Figure 3.15 Schematic model of three EFD elements connected in parallel as defined for simulation in COMSOL. The samples inflow at the bottom surface ( $y = 0$ ) and outflow through the three channels as for the single device considered above.

	Type 2	
Total length (mm)	16	AF
Angle (degree)	45	theta(<DEF)
Injection width (mm)	2	A1A2
Main width (mm)	2	F1F2
Length_AB (mm)	9	AB
Length_BC (mm)	6	BC
Height (mm)	2	height
Width_branch (mm)	1	C1D1
distance between element(mm)	15	
	Pattern 2	
A1B1	Vn	
A2B2	Vp	
B1C1	Vn	
B2C2	Vp	
D1E1	Vg	
D2E2	Vg	
Vp(Volt)	10,15,20	
Vn(Volt)	-10,-15,-20	
Vg(Volt)	0	

Table 3.3 Dimensions and parameter settings for the model of three EFD devices in parallel.

The model will be studied by increasing the bi-polar voltage of the plates from  $\pm 10\text{V}$ ,  $\pm 15\text{V}$  to  $\pm 20\text{V}$ , all of the other parameters and conditions will be kept unchanged (as listed in Table 3.3). The working fluid tested is again the net neutral sample with NaCl in water solution.

### 3.3.2 Results and discussion

The average concentration at the cross-sectional surfaces at the very end of the exit channels were plotted in Figures 3.16 to 3.18. It should be noted that "channel 1" denotes channel 1 of the element on the very left; "channel 2" denotes the channel 2 of the element on the very left; "channel 3" denotes the channel 3 of the element on the very right.

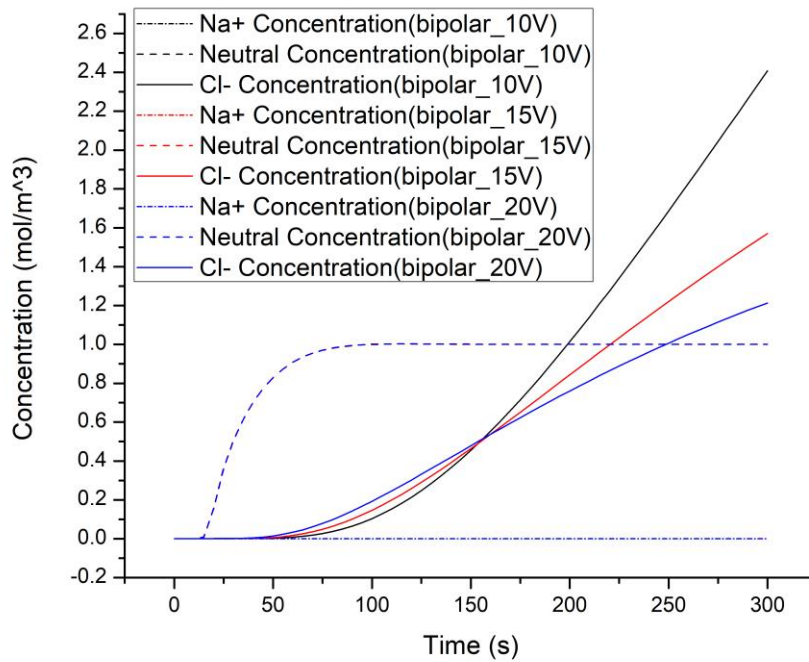


Figure 3.16 Average concentrations at the very end of the side exit channel 1 (cross-sectional) based on different electric potentials applied to the electrodes. The electrode voltages were  $V = \pm 10\text{V}$ ,  $\pm 15\text{V}$  and  $\pm 20\text{V}$ .

Figure 3.16 shows that the chloride ions (solid lines) in all cases migrate towards channel 1 while the sodium ions do not (short dash lines), as expected. As with the single devices studied earlier, the neutral component reaches a plateau quickly (within 100 sec) in all cases such that all of the lines are overlapped (a stronger electric field ( $\vec{E} = -\nabla V$ ) will not affect the migration of the neutral component). Also as mentioned in the previous section, a stronger electric field results in a relative stronger effect of the non-diffusional velocities;  $\frac{\partial c}{\partial t}$  becomes smaller, which is why the slope in the Figure 3.16 decreases.

Additionally, the intersection point (chloride ion line with the neutral component line) appears later when the electric potential is higher. The stronger electric field strength ( $\vec{E} = -\nabla V$ ) causes the ionic components to be pulled stronger toward the electrodes causing the chloride ions longer to migrate toward the side exit channel.

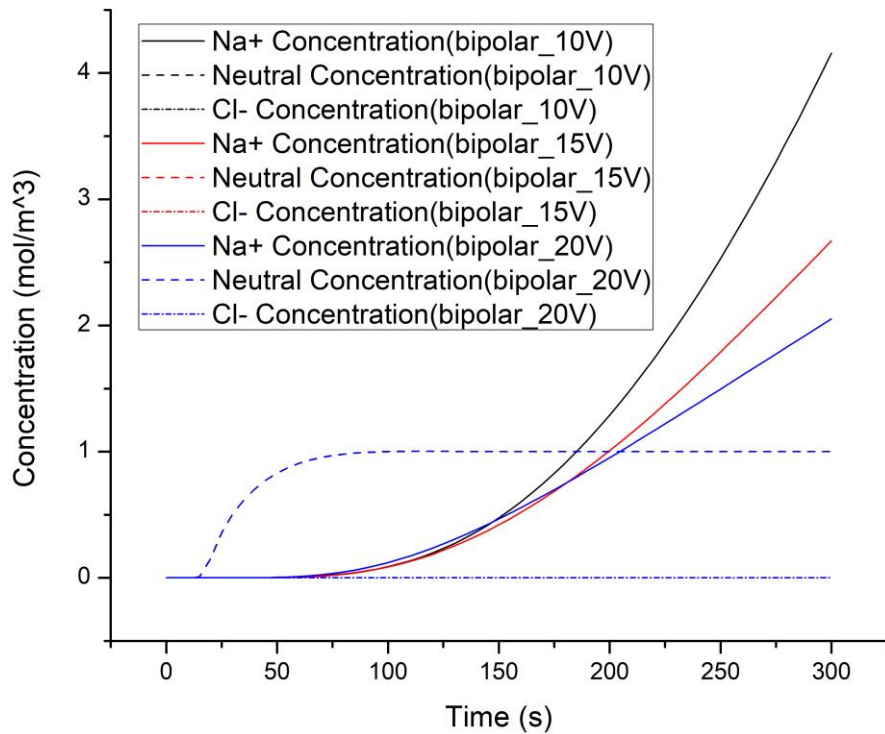
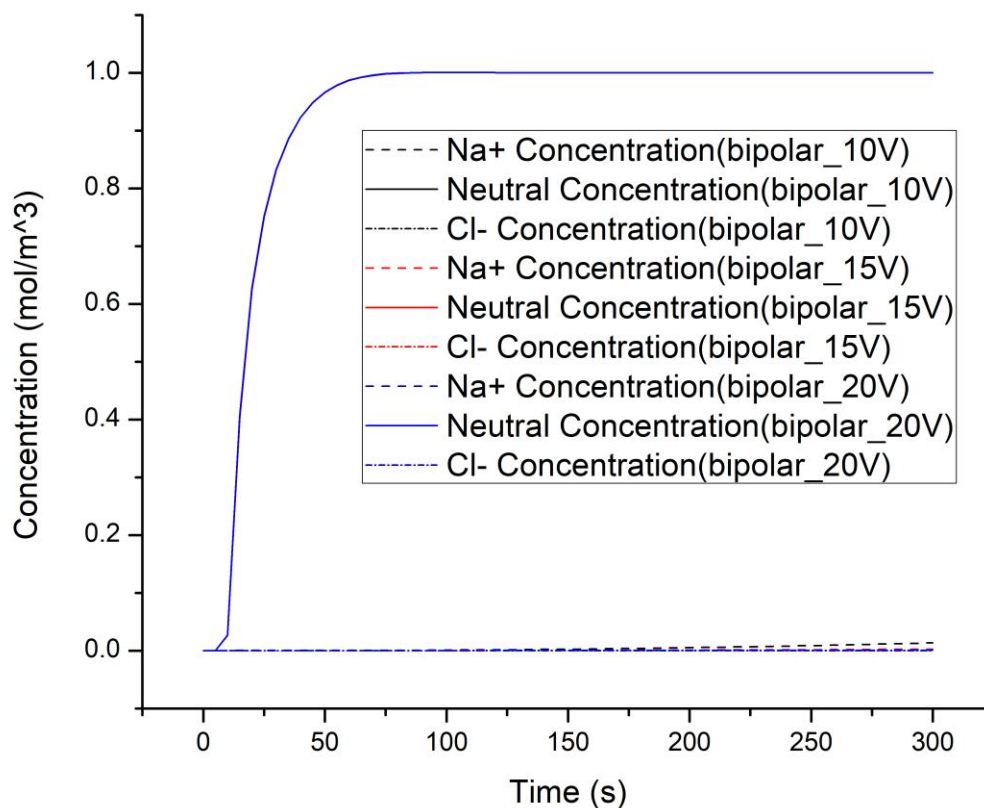


Figure 3.17 Average concentrations at the very end of the side exit channel 3 (cross-sectional) based on different electric potential applied to the electrodes. The electrode voltages were  $V = \pm 10V$ ,  $\pm 15V$  and  $\pm 20V$ .

Similarly, Figure 3.17 shows the average concentration over the cross-sectional area at the very end of channel 3. The sodium ions in all cases migrate to channel 3, as expected. Again, the migration behaviors of the sodium ions ( $Na^+$ ) and chloride ions ( $Cl^-$ ) are not the same due to different diffusion coefficients.



**Figure 3.18 Average concentrations at the very end of the main exit channel 2 (cross-sectional) based on different electric potential applied to the electrodes. The electrode voltages were  $V = \pm 10V$ ,  $\pm 15V$  and  $\pm 20V$ .**

Figure 3.18 shows the migration behaviors of the three components in the main exit channel (channel 2). Again, all the neutral component lines are overlapped, and all the other component lines are nearly zero, which means that no ionic components outflow from this channel. This result again agrees with the expectation that the analytes are desalted.

### 3.4 Multi-element EFD in parallel with a longer injection channel length vs electric potential

#### 3.4.1 Introduction

It has been shown that the desalination process can be carried out using three elements connected in series. In order to investigate effects that may allow optimization of the performance, it is worthwhile to explore some other geometries of the model by adjusting the dimensions, for example the injection channel length and width. Here, the same three elements shown in Figure 3.15 were used; the new dimensions and parameter settings are listed in Table 3.4 below.

	Type 2	
Total length (mm)	21	AF
Angle (degree)	45	theta(<DEF)
Injection width (mm)	2	A1A2
Main width (mm)	2	F1F2
Length_AB (mm)	14	AB
Length_BC (mm)	6	BC
Height (mm)	2	height
Width_branch (mm)	1	C1D1
distance between element(mm)	15	
	Pattern 2	
A1B1	Vn	
A2B2	Vp	
B1C1	Vn	
B2C2	Vp	
D1E1	Vg	
D2E2	Vg	
Vp(Volt)	10,15,20	
Vn(Volt)	-10,-15,-20	
Vg(Volt)	0	

**Table 3.4 Dimensions and parameter settings used to define the model of the three EFD devices in parallel with a longer injection length. The changes are highlighted in green.**

This variant of the model will be examined by increasing the bi-polar voltage of the plates from  $\pm 10V$ ,  $\pm 15V$  to  $\pm 20V$ , all other parameters and conditions will be kept unchanged (as listed in Table 3.4). The working fluid tested is again the net neutral sample with NaCl in water solution.

### 3.4.2 Results and discussion

The average component concentration at the cross-sectional surface at the very end of the exit channels were plotted in Figures 3.19 to 3.21.

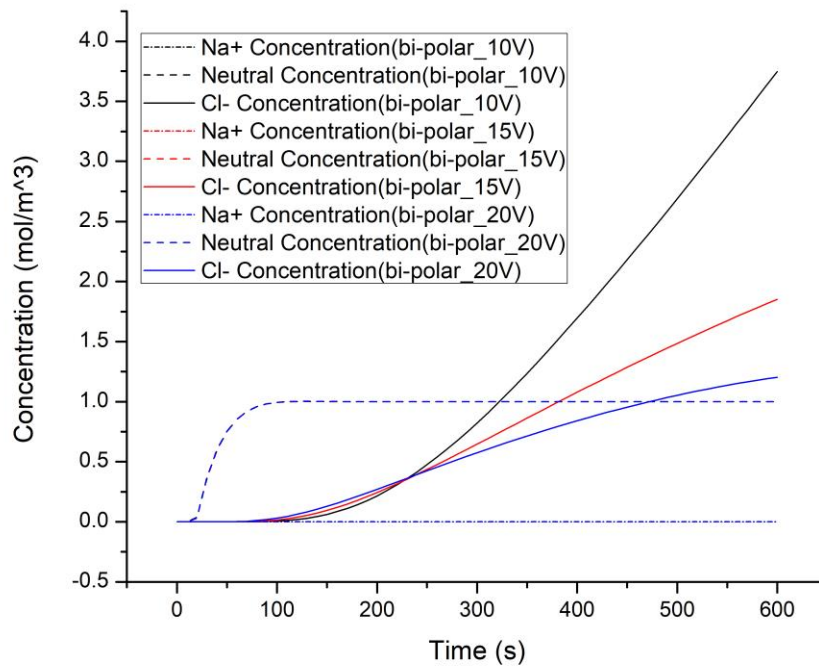
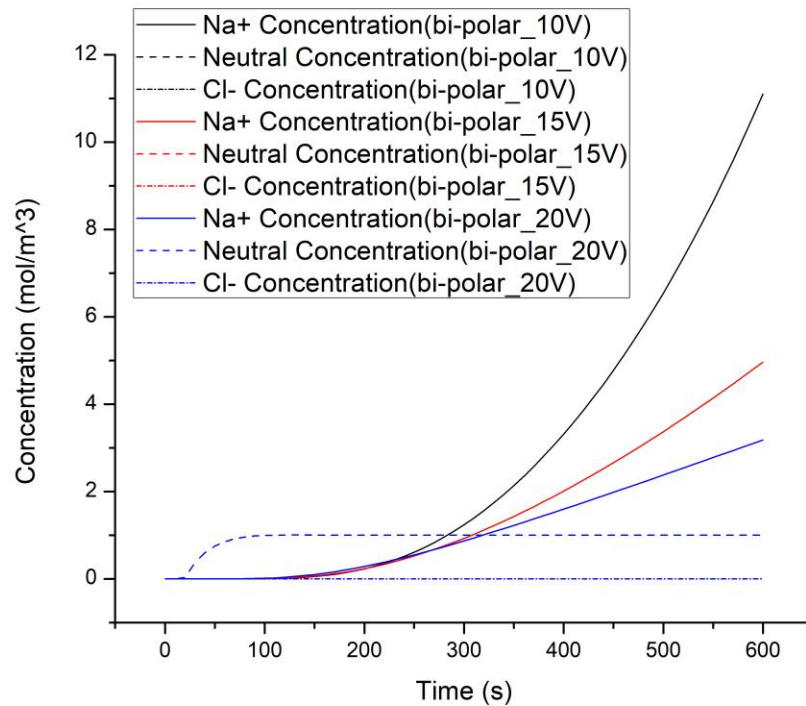


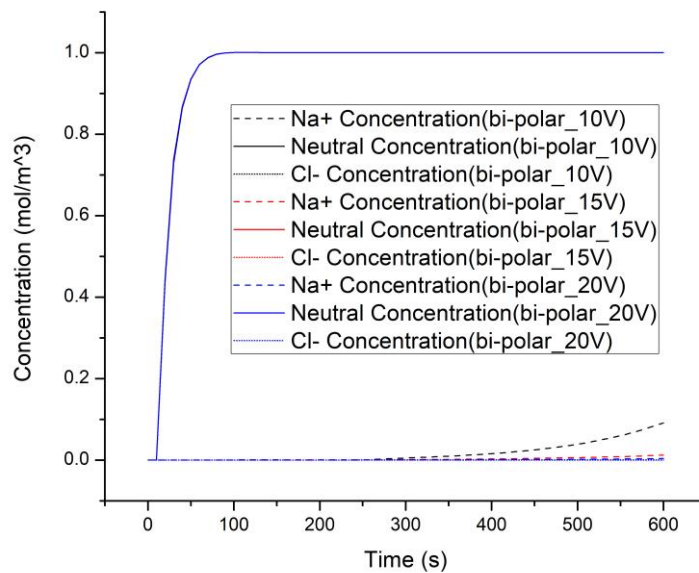
Figure 3.19 Average concentrations at the very end of the side exit channel 1 based on different electric potentials applied to the electrodes for the case of a longer injection channel length. The electrode voltages were  $V = \pm 10V$ ,  $\pm 15V$  and  $\pm 20V$ .

Figure 3.19 shows that the model with a longer injection channel length exhibits qualitatively similar behavior to that shown previously in Figure 3.16. Similarly, Figure 3.20 below shows qualitatively similar behavior to that shown previously in Figure 3.17. Therefore, the longer injection length does not affect the trends observed previously. The only difference that could be observed is the intersection point. It is found that the intersection point appears earlier in the case of shorter injection length than for the case of the longer length (under the same conditions), which could be explained by the expectation that a longer injection channel results in a longer time to migrate.



**Figure 3.20** Average concentration at the very end of the side exit channel 3 based on different electric potentials applied to the electrodes for the case of a longer injection channel length). The electrode voltages were  $V = \pm 10V$ ,  $\pm 15V$  and  $\pm 20V$ .

Figure 3.21 shows the migration behaviors of the three components in the main exit channel (channel 2). Again, all the neutral component lines are overlapped, but here the ionic components (e.g. sodium ions in case  $\pm 10V$ ) appear, which is not desirable. Therefore, it suggests that a longer injection channel might not always yield the best performance. There is evidently a trade-off between the effects of the different fields. The possible reason why the ionic components outflow from main exit channel for this geometry is that a relatively weaker electric field (at the injection channel side) may not be able to retard the ions outflow. The ions in channel 2 are the overflow from the side channel, which results from the corresponding side of the channel electrodes being set at ground rather than any non-zero electric potential.



**Figure 3.21 Average concentration at the very end of the main exit channel 2 based on different electric potentials applied to the electrodes for the case of a longer injection channel length. The electrode voltages were  $V = \pm 10V$ ,  $\pm 15V$  and  $\pm 20V$ .**

### 3.5 Multi-element EFD in parallel with injection channel width changed vs electric potential

#### 3.5.1 Introduction

Here, the same model with three elements connected in parallel (as shown in Figure 3.15) was used but with a different injection channel width; the new dimensions and parameter settings are listed in Table 3.5 below.

	Type 2	
Total length (mm)	16	AF
Angle (degree)	45	theta(<DEF)
Injection width (mm)	4	A1A2
Main width (mm)	2	F1F2
Length_AB (mm)	9	AB
Length_BC (mm)	6	BC
Height (mm)	2	height
Width_branch (mm)	1	C1D1
distance between element(mm)	15	
	Pattern 2	
A1B1	Vn	
A2B2	Vp	
B1C1	Vn	
B2C2	Vp	
D1E1	Vg	
D2E2	Vg	
Vp(Volt)	10,15,20	
Vn(Volt)	-10,-15,-20	
Vg(Volt)	0	

**Table 3.5 Dimensions and parameter settings for the model of three EFD devices in parallel with injection width changed. The changes are highlighted in green.**

The model will be investigated by increasing the bi-polar voltage of the plates from  $\pm 10V$ ,  $\pm 15V$  to  $\pm 20V$ , all the other parameters and conditions will be kept unchanged (as listed in Table 3.5). The working fluid tested is again the net neutral sample with NaCl in water solution.

### 3.5.2 Results and discussion

The average concentrations at the cross-sectional surfaces at the very end of the exit channels (same notation as used in sections 3.3 and 3.4) were plotted separately in the following figures.

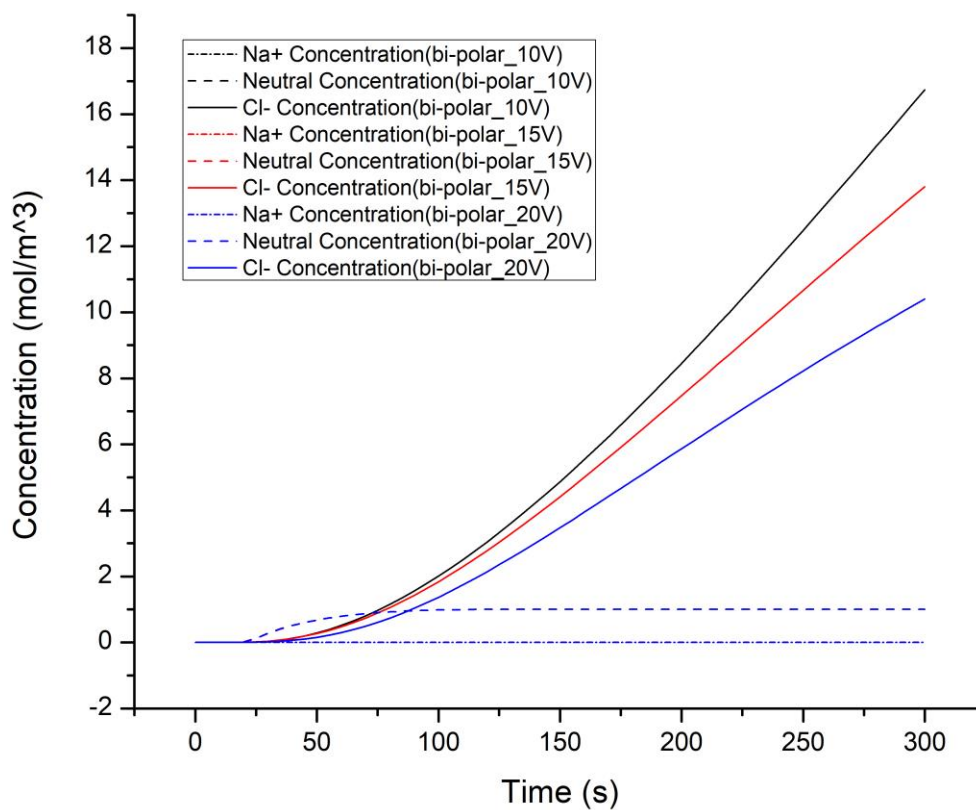
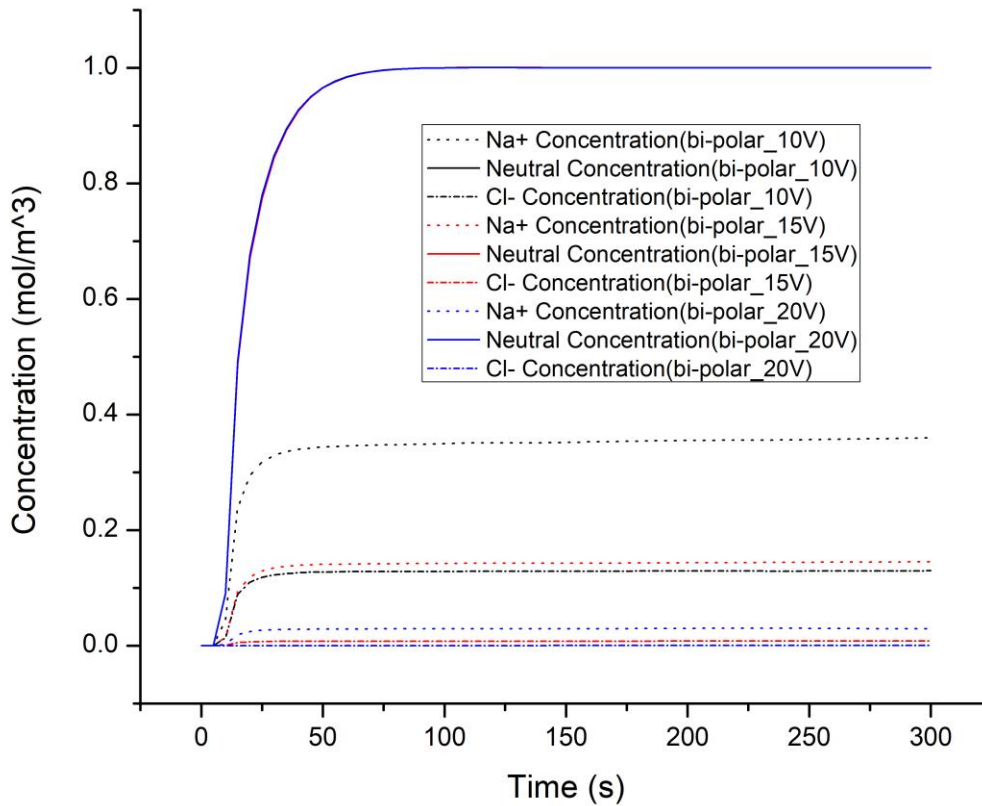


Figure 3.22 Average concentrations at the very end of the side exit channel 1 based on different electric potentials applied to the electrodes for the case where the injection channel width is larger. The electrode voltages are  $V = \pm 10V$ ,  $\pm 15V$  and  $\pm 20V$ .

The profiles plotted in Figure 3.22 exhibit the same qualitative behavior as those shown in Figure 3.16. Therefore, the wider injection width does not appear to affect the trends that were observed previously (including the intersection point).



**Figure 3.23 Average concentrations at the very end of the main exit channel 2 based on different electric potentials applied to the electrodes for the case where the injection channel width is larger. The electrode voltages were  $V = \pm 10V$ ,  $\pm 15V$  and  $\pm 20V$ .**

Figure 3.23 shows the migration behaviors of the three components in the main exit channel (channel 2). Again, all the neutral component lines are overlapped, but here the other components were not reduced to nearly zero, which means that they all outflow from this

channel. Evidently, the wider injection channel may lead to an overflow problem on the main exit channel if the electric field is not strong enough. Thus, when considering the adjustment of the design geometry for such EFD devices, the injection channel width might be difficult to optimize.

## Chapter 4: Conclusions and Suggestions for Future Work

### 4.1 Conclusions

In this study, mass transport of solutes in electro-fluidic-dynamic devices in one dimension (1D) and two dimensions (2D) for separation were investigated by carrying out device simulations based on numerical implementation of the theoretical descriptions.

For the 1D-EFD device, a simulation model was built to study the impact due to an externally applied pressure during the process of capillary electrophoresis (CE). Adding external pressure during this process usually contributes to band broadening, especially if the pressure induced flow is significant. The resolution is normally negatively affected in pressure-assisted capillary electrophoresis (PACE). Frontal analysis (FA), however, can potentially benefit from using an external pressure while avoiding the drawbacks seen in other modes of CE, because it doesn't require peaks to be baseline separated. Under a typical CE-FA set-up, it was found that the detected concentrations of analyte will not be significantly affected by an external pressure less than 5 psi, which means that this technique is suitable for some CE applications. Besides, the measured ligand concentration in PACE-FA was also not affected by common variables like molecular diffusion coefficient ( $10^{-8} \text{ m}^2 / \text{s}$  to  $10^{-11} \text{ m}^2 / \text{s}$ ) and capillary length. Moreover, to provide an experimental verification of the simulation results, PACE-FA was used to study the binding interactions between hydroxypropyl  $\beta$ -cyclodextrin (HP- $\beta$ -CD) and small ligand molecules. Taking the HP- $\beta$ -CD /benzoate pair as an example, the binding constants determined by CE-FA ( $18.3 \pm 0.8 \text{ M}^{-1}$ ) and PACE-FA ( $16.5 \pm 0.5 \text{ M}^{-1}$ ) are found to be similar. Based on these experimental results, it is concluded that PACE-FA can reduce the time of binding analysis while maintaining the accuracy of the measurements. Since this technique is applicable to most small molecules as well as those larger biological molecules with bioactive conformations that

require the presence of other co-factors, PACE-FA could become a more common tool for the analysis of bio-molecular interactions. With similar applicability, PACE-FA brings significant improvements to the conventional CE-FA technique. The simulation was based on COMSOL Multiphysics®, which proved to be a useful numerical analysis tool for this study.

For the 2D-EFD devices, it was found from the simulation studies that such devices might offer a promising alternative for sample desalination applications such as sample pretreatment for the mass spectrometry. From the simulation results presented in chapter 3, the migration of solute components during the process of desalination on a single EFD device and on multi-element EFD devices can be observed. The ionic components could be separated and directed into the specific (side-arm) exit channels to yield a desalted outflow stream in the main exit channel (designated channel 2). Various geometries, as well as the strength and pattern of the applied electric field were studied, and it can be concluded that the stronger applied electrical field helps to improve the performance of the desalination and the optimization of the EFD device depends on the geometric design of the device relatively heavily. But, for now, the proposed design used in chapter 3 provides a sufficient basis for a real 2D-EFD to be fabricated and tested.

## **4.2 Future work**

The migration of solute components during the process of the desalination on EFD device can be numerically simulated using COMSOL Multiphysics and the design of a real device can proceed and be tested experimentally. The EFD device chip can be fabricated using polydimethylsiloxane (PDMS) (Sylard184, Dow Corning, Midland MI) with a 3D-printer. The positive potentials at the electrodes can be applied by power supplies and the pressure-induced

velocity can be precisely controlled using a syringe pump to achieve the required conditions. The charged-particle or inorganic solutions can be visualized by fluorescence microscopy. A microscope can be used (e.g. Nikon Eclipse 80i) and the fluorescence signals can be recorded by a high-definition color charge coupled device (CCD) camera. When it is necessary to monitor the migration behaviors of the analytes in the future, an optical imaging system with dual-view filters can also be home built. The excitation wavelength would depend on the fluorophore/analyte combinations studied.

One problem that may be encountered during the measurement is the formation of bubbles produced in the channel which could cause the channel to become blocked without any visible signs. This can be addressed by making adjustments to the parameter settings using the simulation tool COMSOL. Once a working device is available to be tested, the parameter settings should be re-studied and the tradeoffs between the shorter length of the channel and the higher electric field strength should be investigated in order to point the way toward an optimal design.

Similarly, the multi-element EFD experiment can be regarded as an extension of the EFD desalination device with a different geometry. It is also worthwhile to explore the performance of such devices with other ions like  $\text{SO}_4^{2-}$  and  $\text{Cu}^{2+}$ . In this case, most of the experimental setting and methodology can be the same as mentioned earlier. The charged-particle or inorganic solutions can be monitored by conductivity detection, perhaps having several conductivity meters at the exit channel ends to monitor the concentration.

The simulations studied in chapter 3 are investigated mostly based on Type 2 while they all can also be based on a Type 1 device as depicted in Figure 3.2. The parameters of the design (including the experimental settings, like voltage input) value are still worthy to be discussed and

adjusted before proceeding with the experimental measurements. Specifically, the injection pressure, flowrate and the electric field strength, as well as the electrode pattern, are to be optimized, not only before the experiment but also during the measurement. These works can still be simulated using the existing COMSOL models without needing to change too much.

## Bibliography

- [1] C. Liu, Y. Luo, E. Jane Maxwell, N. Fang, and D. D. Y. Chen, “Reverse of mixing process with a two-dimensional electro-fluid-dynamic device,” *Anal. Chem.*, vol. 82, no. 6, pp. 2182–2185, 2010.
- [2] C. Liu, Y. Luo, N. Fang, and D. D. Y. Chen, “Analyte distribution at channel intersections of electro-fluid-dynamic devices,” *Anal. Chem.*, vol. 83, no. 4, pp. 1189–1192, 2011.
- [3] C. Liu, Y. Luo, E. J. Maxwell, N. Fang, and D. D. Y. Chen, “Potential of two-dimensional electro-fluid-dynamic devices for continuous purification of multiple components from complex samples,” *Analytical Chemistry*, vol. 83, no. 21, pp. 8208–8214, 2011.
- [4] C. Liu and D. D. Y. Chen, “Comparison of sample introduction methods for continuous chemical purification in two-dimensional electro-fluid-dynamic devices,” *Analytical Chemistry*, vol. 86, no. 22, pp. 11380–11386, 2014.
- [5] D. Chen, H. R. Harke, and N. J. Dovichi, “Two-label peak-height encoded DNA sequencing by capillary gel electrophoresis: Three examples,” *Nucleic Acids Res.*, vol. 20, no. 18, pp. 4873–4880, 1992.
- [6] H. Swerdlow *et al.*, “Three DNA sequencing methods using capillary gel electrophoresis and laser-induced fluorescence,” *Anal. Chem.*, vol. 63, no. 24, pp. 2835–41, 1991.
- [7] M. Shannon, P. W. Bohn, M. Elimelech, J. G. Georgiadis, B. J. Mariñas, and A. M. Mayes, “Science and technology for water purification in the coming decades,” *Nature*, vol. 452, no. March, pp. 301–310, 2008.
- [8] N. Ghaffour, T. M. Missimer, and G. L. Amy, “Technical review and evaluation of the economics of water desalination : Current and future challenges for better water supply sustainability,” *DES*, vol. 309, no. 2013, pp. 197–207, 2015.

- [9] “National oceanographic data center.” [Online]. Available: <https://www.nodc.noaa.gov/>.
- [10] “Brackish ground water,” *National ground water association*. .
- [11] A. D. Khawaji, I. K. Kutubkhanah, and J. Wie, “Advances in seawater desalination technologies,” vol. 221, pp. 47–69, 2008.
- [12] Q. Schiermeier, “Water: Purification with a pinch of salt,” *Nature*, vol. 452:260–26, 2008.
- [13] M. A. Anderson, A. L. Cudero, and J. Palma, “Capacitive deionization as an electrochemical means of saving energy and delivering clean water. Comparison to present desalination practices: Will it compete?,” *Electrochim. Acta*, vol. 55, no. 12, pp. 3845–3856, 2010.
- [14] D. Energy, M. Elimelech, and W. A. Phillip, “The Future of Seawater and the Environment,” vol. 333, no. August, pp. 712–718, 2011.
- [15] F. A. AlMarzooqi, A. A. Al Ghaferi, I. Saadat, and N. Hilal, “Application of Capacitive Deionisation in water desalination: A review,” *Desalination*, vol. 342, pp. 3–15, 2014.
- [16] L. F. Greenlee, D. F. Lawler, B. D. Freeman, B. Marrot, P. Moulin, and P. Ce, “Reverse osmosis desalination : Water sources , technology , and today ’ s challenges,” *Water Res.*, vol. 43, no. 9, pp. 2317–2348, 2009.
- [17] H. Strathmann, “Electrodialysis, a mature technology with a multitude of new applications,” *Desalination*, vol. 264, no. 3, pp. 268–288, 2010.
- [18] S. Song, A. K. Singh, T. J. Shepodd, and B. J. Kirby, “Microchip Dialysis of Proteins Using in Situ Photopatterned Nanoporous Polymer Membranes,” *Anal. Chem.*, vol. 76, no. 8, pp. 2367–2373, 2004.
- [19] N. Xu, Y. Lin, S. A. Hofstadler, D. Matson, C. J. Call, and R. D. Smith, “A Microfabricated Dialysis Device for Sample Cleanup in Electrospray Ionization Mass

- Spectrometry,” *Anal. Chem.*, vol. 70, no. 17, pp. 3553–3556, 1998.
- [20] F. Xiang, Y. Lin, J. Wen, D. W. Matson, and R. D. Smith, “An integrated microfabricated device for dual microdialysis and on-line ESI-ion trap mass spectrometry for analysis of complex biological samples,” *Anal. Chem.*, vol. 71, no. 8, pp. 1485–1490, 1999.
- [21] R. Kwak, G. Guan, W. K. Peng, and J. Han, “Microscale electro dialysis: Concentration profiling and vortex visualization,” *Desalination*, vol. 308, pp. 138–146, 2013.
- [22] M. E. Suss, P. M. Biesheuvel, T. F. Baumann, M. Stadermann, and J. G. Santiago, “In situ spatially and temporally resolved measurements of salt concentration between charging porous electrodes for desalination by capacitive deionization,” *Environ. Sci. Technol.*, vol. 48, no. 3, pp. 2008–2015, 2014.
- [23] O. N. Demirer and C. H. Hidrovo, “Laser-induced fluorescence visualization of ion transport in a pseudo-porous capacitive deionization microstructure,” *Microfluid. Nanofluidics*, vol. 16, no. 1–2, pp. 109–122, 2014.
- [24] B. D. MacDonald, M. M. Gong, P. Zhang, and D. Sinton, “Out-of-plane ion concentration polarization for scalable water desalination,” *Lab Chip*, vol. 14, no. 4, pp. 681–685, 2014.
- [25] S. J. Kim, Y. A. Song, and J. Han, “Nanofluidic concentration devices for biomolecules utilizing ion concentration polarization: Theory, fabrication, and applications,” *Chem. Soc. Rev.*, vol. 39, no. 3, pp. 912–922, 2010.
- [26] N. Lion, V. Gobry, H. Jensen, J. S. Rossier, and H. Girault, “Integration of a membrane-based desalting step in a microfabricated disposable polymer injector for mass spectrometric protein analysis,” *Electrophoresis*, vol. 23, no. 20, pp. 3583–3588, 2002.
- [27] D. Gao, H. Liu, Y. Jiang, and J. M. Lin, “Recent advances in microfluidics combined with mass spectrometry: Technologies and applications,” *Lab Chip*, vol. 13, no. 17, pp. 3309–

- 3322, 2013.
- [28] Y. Oren, “Capacitive deionization (CDI) for desalination and water treatment - past, present and future (a review),” *Desalination*, vol. 228, no. 1–3. pp. 10–29, 2008.
- [29] S. J. Seo *et al.*, “Investigation on removal of hardness ions by capacitive deionization (CDI) for water softening applications,” *Water Research*, vol. 44, no. 7. pp. 2267–2275, 2010.
- [30] A. Subramani and J. G. Jacangelo, “Emerging desalination technologies for water treatment: A critical review,” *Water Research*, vol. 75. pp. 164–187, 2015.
- [31] S. J. Kim, S. H. Ko, K. H. Kang, and J. Han, “Direct seawater desalination by ion concentration polarization,” *Nat. Nanotechnol.*, vol. 5, no. 4, pp. 297–301, 2010.
- [32] R. M. Crooks, R. K. Anand, U. Tallarek, K. N. Knust, and D. Hlushkou, “Electrochemically Mediated Seawater Desalination,” *Angew. Chemie Int. Ed.*, vol. 52, no. 31, pp. 8107–8110, 2013.
- [33] E. Bakker *et al.*, “Coulometric Sodium Chloride Removal System with Nafion Membrane for Seawater Sample Treatment,” *Anal. Chem.*, vol. 84, no. 14, pp. 6158–6165, 2012.
- [34] D. Chen and C. Liu, “Devices and Methods for Processing Fluid Samples,” US20170212076A1.
- [35] J. W. Jorgenson and K. D. Lukacs, “Capillary zone electrophoresis,” *Science (80-. )*, vol. 222, pp. 266–274, 1983.
- [36] R. Weinberger, E. Sapp, and S. Moring, “Capillary electrophoresis of urinary porphyrins with absorbance and fluorescence detection,” *J. Chromatogr. A*, vol. 516, no. 1, pp. 271–285, 1990.
- [37] T. Ohara, A. Shibukawa, and T. Nakagawa, “Capillary electrophoresis/frontal analysis for

- microanalysis of enantioselective protein binding of a basic drug,” *Anal. Chem.*, vol. 67, no. 19, pp. 3520–3525, 1995.
- [38] S. Fanali *et al.*, “Chiral capillary electrophoresis–electrospray mass spectrometry coupling using vancomycin as chiral selector,” *J. Chromatogr. A*, vol. 800, no. 1, pp. 69–76, 1998.
- [39] C. E. Sanger-van de Griend, K. Groningsson, and T. Arvidsson, “Enantiomeric separation of a tetrapeptide with cyclodextrin extension of the model for chiral capillary electrophoresis by complex formation of one enantiomer molecule with more than one chiral selector molecules,” *J. Chromatogr. A*, vol. 782, no. 2, pp. 271–279, 1997.
- [40] S. D. Mendonsa and M. T. Bowser, “In Vitro Selection of High-Affinity DNA Ligands for Human IgE Using Capillary Electrophoresis,” *Anal. Chem.*, vol. 76, no. 18, pp. 5387–5392, 2004.
- [41] K. Harada, E. Fukusaki, and A. Kobayashi, “Pressure-assisted capillary electrophoresis mass spectrometry using combination of polarity reversion and electroosmotic flow for metabolomics anion analysis,” *J. Biosci. Bioeng.*, vol. 101, no. 5, pp. 403–409, 2006.
- [42] N. L. Kuehnbaum, A. Kormendi, and P. Britz-McKibbin, “Multisegment Injection-Capillary Electrophoresis-Mass Spectrometry: A High-Throughput Platform for Metabolomics with High Data Fidelity,” *Anal. Chem.*, 2013.
- [43] Y. Zhao *et al.*, “Coupling Capillary Zone Electrophoresis with Electron Transfer Dissociation and Activated Ion Electron Transfer Dissociation for Top-Down Proteomics,” *Anal. Chem.*, 2015.
- [44] J. C. Kraak, S. Busch, and H. Poppe, “Study of protein-drug binding using capillary zone electrophoresis,” *J. Chromatogr. A*, vol. 608, no. 1–2, pp. 257–264, 1992.
- [45] A. Shibukawa, Y. Kuroda, and T. Nakagawa, “High-performance frontal analysis for

- drug–protein binding study,” *J. Pharm. Biomed. Anal.*, vol. 18, no. 6, pp. 1047–1055, 1999.
- [46] N. Sisavath, L. Leclercq, T. Le Saux, F. Oukacine, and H. Cottet, “Study of interactions between oppositely charged dendrigraft poly-L-lysine and human serum albumin by continuous frontal analysis capillary electrophoresis and fluorescence spectroscopy,” *J. Chromatogr. A*, vol. 1289, pp. 127–132, 2013.
- [47] N. Sisavath, P. Got, G. M. Charrière, D. Destoumieux-Garzon, and H. Cottet, “Taking Advantage of Electric Field Induced Bacterial Aggregation for the Study of Interactions between Bacteria and Macromolecules by Capillary Electrophoresis,” *Anal. Chem.*, vol. 87, no. 13, pp. 6761–6768, 2015.
- [48] C. T. Culbertson and J. W. Jorgenson, “Flow Counterbalanced Capillary Electrophoresis,” *Anal Chem*, vol. 66, no. 7, pp. 955–962, 1994.
- [49] J. M. Miller, A. C. Blackburn, Y. Shi, A. J. Melzak, and H. Y. Ando, “Semi-empirical relationships between effective mobility, charge, and molecular weight of pharmaceuticals by pressure-assisted capillary electrophoresis: Applications in drug discovery,” *Electrophoresis*, vol. 23, no. 17, pp. 2833–2841, 2002.
- [50] H. Wan *et al.*, “High-throughput screening of pKa values of pharmaceuticals by pressure-assisted capillary electrophoresis and mass spectrometry,” *Rapid Commun. Mass Spectrom.*, vol. 17, no. 23, pp. 2639–2648, 2003.
- [51] Z. Jia, T. Ramstad, and M. Zhong, “Medium-throughput pKa screening of pharmaceuticals by pressure-assisted capillary electrophoresis,” *Electrophoresis*, vol. 22, no. 6, pp. 1112–1118, 2001.
- [52] T. Soga, T. Ishikawa, S. Igarashi, K. Sugawara, Y. Kakazu, and M. Tomita, “Analysis of

- nucleotides by pressure-assisted capillary electrophoresis–mass spectrometry using silanol mask technique,” *J. Chromatogr. A*, vol. 1159, no. 1, pp. 125–133, 2007.
- [53] T. Soga, Y. Ueno, H. Naraoka, K. Matsuda, M. Tomita, and T. Nishioka, “Pressure-Assisted Capillary Electrophoresis Electrospray Ionization Mass Spectrometry for Analysis of Multivalent Anions,” *Anal. Chem.*, vol. 74, no. 24, pp. 6224–6229, 2002.
- [54] C. Qian, K. A. Kovalchik, M. S. MacLennan, X. Huang, and D. D. Y. Chen, “Mobility-based correction for accurate determination of binding constants by capillary electrophoresis-frontal analysis,” *Electrophoresis*, vol. 38, no. 12, pp. 1572–1581, 2017.
- [55] S. Fermas, F. Gonnet, A. Varenne, P. Gareil, and R. Daniel, “Frontal Analysis Capillary Electrophoresis Hyphenated to Electrospray Ionization Mass Spectrometry for the Characterization of the Antithrombin/Heparin Pentasaccharide Complex,” *Anal. Chem.*, vol. 79, no. 13, pp. 4987–4993, 2007.
- [56] Y. Sun, S. Cressman, N. Fang, P. R. Cullis, and D. D. Y. Chen, “Capillary Electrophoresis Frontal Analysis for Characterization of  $\alpha v \beta 3$  Integrin Binding Interactions,” *Anal. Chem.*, vol. 80, no. 9, pp. 3105–3111, 2008.
- [57] Z. Jia, T. Ramstad, and M. Zhong, “Determination of protein–drug binding constants by pressure-assisted capillary electrophoresis (PACE)/frontal analysis (FA),” *J. Pharm. Biomed. Anal.*, vol. 30, no. 3, pp. 405–413, 2002.
- [58] D. J. Winzor, “Determination of binding constants by analogous procedures in size exclusion chromatography and capillary electrophoresis,” *Anal. Biochem.*, vol. 383, no. 1, pp. 1–17, Dec. 2008.
- [59] D. J. Winzor, “A need for caution in the use of frontal analysis continuous capillary electrophoresis for the determination of ligand binding data,” *Anal. Biochem.*, vol. 349,

- no. 2, pp. 285–291, Feb. 2006.
- [60] P. H. Paul, M. G. Garguilo, and D. J. Rakestraw, “Imaging of pressure-and electrokinetically driven flows through open capillaries,” *Anal. Chem. DC-*, vol. 70, pp. 2459–2467, 1998.
- [61] G. Taylor, “Dispersion of Soluble Matter in Solvent Flowing Slowly through a Tube,” *Proc. R. Soc. London. Ser. A. Math. Phys. Sci.*, vol. 219, no. 1137, pp. 186–203, 1953.
- [62] M. T. Bowser and D. D. Y. Chen, “The effects of a mixture of charged and neutral additives on analyte migration behavior in capillary electrophoresis,” *Anal. Chem.*, vol. 70, no. 15, pp. 3526–3535, 1998.
- [63] M. T. Bowser and D. D. Y. Chen, “Monte Carlo Simulation of Error Propagation in the Determination of Binding Constants from Rectangular Hyperbolae. 2. Effect of the Maximum-Response Range,” *J. Phys. Chem. A*, vol. 103, no. 1, pp. 197–202, Jan. 1999.
- [64] B. L. H. M. Sperber, M. A. Cohen Stuart, H. A. Schols, A. G. J. Voragen, and W. Norde, “Binding of  $\beta$ -Lactoglobulin to Pectins Varying in their Overall and Local Charge Density,” *Biomacromolecules*, vol. 10, no. 12, pp. 3246–3252, 2009.
- [65] T. Zou, F. Oukacine, T. Le Saux, and H. Cottet, “Neutral Coatings for the Study of Polycation/Multicharged Anion Interactions by Capillary Electrophoresis: Application to Dendrigraft Poly-l-lysines with Negatively Multicharged Molecules,” *Anal. Chem.*, vol. 82, no. 17, pp. 7362–7368, 2010.
- [66] C. Qian, H. Fu, K. A. Kovalchik, H. Li, and D. D. Y. Chen, “Specific Binding Constant and Stoichiometry Determination in Free Solution by Mass Spectrometry and Capillary Electrophoresis Frontal Analysis,” *Anal. Chem.*, vol. 89, no. 17, pp. 9483–9490, 2017.